






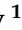




Article

Accurate Decomposition of Galaxies with Spiral Arms: Dust Properties and Distribution

Alexander A. Marchuk ^{1,2,*} , Ilia V. Chugunov ¹ , Frédéric Galliano ³ , Aleksandr V. Mosenkov ⁴ ,
Polina V. Strekalova ¹ , Sergey S. Savchenko ^{1,2} , Valeria S. Kostiuik ⁵ , George A. Gontcharov ¹ ,
Vladimir B. Il'in ^{1,2} , Anton A. Smirnov ¹ and Denis M. Poliakov ¹ 

¹ Central (Pulkovo) Astronomical Observatory, Russian Academy of Sciences, Pulkovskoye Chaussee 65/1, 196140 St. Petersburg, Russia

² St. Petersburg State University, 7/9 Universitetskaya Nab., 199034 St. Petersburg, Russia

³ Université Paris-Saclay, Université Paris Cité, CEA, CNRS, AIM, 91191 Gif-sur-Yvette, France

⁴ Department of Physics and Astronomy, N283 ESC, Brigham Young University, Provo, UT 84602, USA

⁵ Sternberg Astronomical Institute, Lomonosov Moscow State University, Universitetsky Pr. 13, 119234 Moscow, Russia

* Correspondence: a.a.marchuk+astro@gmail.com

Abstract: We analyze three nearby spiral galaxies—NGC 1097, NGC 1566, and NGC 3627—using images from the DustPedia database in seven infrared bands (3.6, 8, 24, 70, 100, 160, and 250 μm). For each image, we perform photometric decomposition and construct a multi-component model, including a detailed representation of the spiral arms. Our results show that the light distribution is well described by an exponential disk and a Sérsic bulge when non-axisymmetric components are properly taken into account. We test the predictions of the stationary density wave theory using the derived models in bands, tracing both old stars and recent star formation. Our findings suggest that the spiral arms in all three galaxies are unlikely to originate from stationary density waves. Additionally, we perform spectral energy distribution (SED) modeling using the hierarchical Bayesian code HerBIE, fitting individual components to derive dust properties. We find that spiral arms contain a significant ($>10\%$) fraction of cold dust, with an average temperature of approximately 18–20 K. The estimated fraction of polycyclic aromatic hydrocarbons (PAHs) declines significantly toward the galactic center but remains similar between the arm and interarm regions.

Keywords: galaxies; spiral structure; galactic dynamics and kinematics; spiral arms; photometric decomposition; dust in galaxies



Academic Editor: Carlo Nipoti

Received: 28 February 2025

Revised: 31 March 2025

Accepted: 5 April 2025

Published: 9 April 2025

Citation: Marchuk, A.A.; Chugunov, I.V.; Galliano, F.; Mosenkov, A.V.; Strekalova, P.V.; Savchenko, S.S.; Kostiuik, V.S.; Gontcharov, G.A.; Il'in, V.B.; Smirnov, A.A.; et al. Accurate Decomposition of Galaxies with Spiral Arms: Dust Properties and Distribution. *Galaxies* **2025**, *13*, 39. <https://doi.org/10.3390/galaxies13020039>

Copyright: © 2025 by the authors. Licensee MDPI, Basel, Switzerland. This article is an open access article distributed under the terms and conditions of the Creative Commons Attribution (CC BY) license (<https://creativecommons.org/licenses/by/4.0/>).

1. Introduction

Dust plays a crucial role in the evolution of a galaxy, although comprising less than 1% of a galaxy's total mass. It absorbs and scatters starlight, then re-emits the absorbed energy in the far-infrared (FIR), causing thermal dust emission to dominate the spectral energy distribution (SED) at wavelengths longer than 10 μm [1]. Dust is also a key tracer of the interstellar gas content, facilitating the formation of molecular hydrogen and other molecules by shielding them from ionizing radiation and acting as a catalyst for chemical reactions [2,3]. For these reasons, dust is intricately linked to ongoing star formation, serving as both a tracer of star-forming regions [4,5] and an active participant in the process by regulating the thermal balance of the interstellar medium (ISM) and contributing to molecule formation [6]. Dust appears in various forms, including a diffuse component

spread throughout the ISM [7], dust lanes along spiral arms and bars [8], and dense, cold molecular clouds associated with star formation [9]. Thus, dust exhibits a vast range of physical properties that must be studied to fully understand its critical role in the formation and evolution of the ISM.

With the ability to now measure dust properties in galaxies up to $z \sim 7$ [10,11]—and even farther thanks to ALMA and JWST—our understanding of dust characteristics in the local Universe has significantly advanced (see reviews in [12,13]). However, key knowledge gaps remain, including the fundamental question of dust grain composition and several unresolved issues in dust evolution and distribution. One major challenge is the dust energy balance problem, where observed FIR–submillimeter (submm) emission appreciably exceeds predictions based on observed dust attenuation [14–19]. This discrepancy suggests that current models of dust emissivity and radiative transfer (RT) may require revision. Another key issue relates to dust heating mechanisms. While the old stellar population has been found to play a significant role in heating dust [20–22], the efficiency of this process depends on the morphological component in which the dust resides, with variations observed between different galaxy structures. Additionally, recent studies have revealed that large-scale dust distributions in galaxies are not purely exponential as once assumed [23,24]. Instead, many galaxies exhibit significant central dust depletion, indicating a more complex dust structure [25,26]. These findings highlight the need for more detailed modeling of dust distribution and heating processes to fully understand the role of dust in galaxy evolution.

These challenges have been addressed using a variety of advanced methods. One of the most effective techniques for examining dust distribution based on observed dust attenuation in edge-on galaxies is RT modeling. By assuming a predefined geometry for each component [22,27–30] or by adopting an azimuthally averaged approach [31,32], radiative transfer calculations can generate sophisticated models. These models are derived either from monochromatic images [33–35] or from multiple bands simultaneously, as implemented in the Monte Carlo-based SKIRT code [36,37].

The evolution of dust content in galaxies has been explored via SED fitting at both unresolved [38–40] and, less frequently, resolved [41–45] scales. Various tools, including CIGALE [46], *piXedfit* [43], MAGPHYS [47], FAST [48], and HerBIE [49], along with modern dust grain models such as THEMIS [50] and the ‘astrodust’-based model [51], have facilitated the study of the relationship between dust content and key galactic properties, including gas abundance, metallicity, stellar mass, and star formation rate [21,38,52,53].

The photometric decomposition of individual galactic subsystems, such as the central bulge or the extended disk, enables a detailed examination of dust and stellar distributions on galactic scales, providing insights into their geometry and spatial distribution. This analysis is typically performed using tools like IMFIT [54] or GALFIT [55], which employ standard parametric functions, such as the Sérsic function for the bulge and an exponential function for the disk. At the same time, the presence of dust hampers photometric analysis because it is not taken into account in a self-consistent manner, and needs manual masking or techniques that work in a limited number of situations [56]. Nevertheless, photometric decomposition has proven to be a valuable technique in both RT [29] and SED [57] modeling, offering crucial insights into the interplay between dust and stellar components in galaxies.

Spiral galaxies are the most numerous type of non-dwarf galaxy in the local Universe [58,59] and remain abundant even at high redshifts ([60,61], and also [62]). Spiral arms, which emit a significant fraction of galactic light [63–65], are optically thick in contrast to the optically thin interarm regions [66] and play a crucial role in shaping the chemical composition of galaxies on large scales [67]. However, their proper inclusion in RT and SED models remains rare.

In RT models, spiral arms are often approximated by an additional disk component [32,68], with some exceptions [23,69], where authors have demonstrated a clear preference for models that explicitly incorporate a spiral structure. Given that the star-to-dust geometry has been shown to be a critical factor in RT modeling [70], properly accounting for spiral arms is essential. It is therefore unsurprising that existing models that omit this attribution often deviate from observed images, particularly in spiral arms and features associated with them, such as “bumps” in azimuthal profiles [22,71,72].

In SED fitting, dust properties in spiral arms can be studied using resolved maps, but such studies are generally limited to a small number of objects due to the significant computational effort required. Additionally, arms must still be properly delineated [45,73]. Alternatively, models can be constructed for individual galactic components [57,74] but, to our knowledge, such an approach has never been applied specifically to spiral arms. This omission is largely due to the difficulty of accurately modeling spiral arms in photometric decomposition studies, where, so far, only the GALFIT approach with Fourier and bending modes, modified by a rotation function, produces some adequately modeled arms [55,75].

In the series of papers [60,64,65], we addressed these issues and introduced a new photometric model that represents individual spiral arms. The model is highly flexible and has been refined throughout our investigation, allowing for significant variation in both arm shape and the light distribution along and across the arm.

In the first paper of this series, the model was applied to 29 galaxies using 3.6 μm band images [76], revealing a connection between the pitch angle and bulge/bar fraction, as well as an increase in the spiral-to-total light ratio in more luminous disks. In the second paper [64], we focused on the iconic galaxy M51, utilizing a wide wavelength range from far-ultraviolet (FUV) to far-infrared, with a total of 17 images from the DustPedia project [77]. By tracing different stellar populations, we tested for the presence of angular offsets associated with the density wave theory [78], examined how spiral pattern properties vary with wavelength, and highlighted the importance of an accurate bulge and disk model. In M51, we do not observe the signs of a long-lived density wave in the whole spiral pattern.

In the final paper of the series [60], we applied the model to a significantly larger sample of 159 galaxies, using data from the HST COSMOS [79], JWST CEERS [80], and JADES [81] surveys. Spanning a wide redshift range of $0.1 \leq z \leq 3.3$, the model was applied to images in optical and near-infrared rest-frame wavelengths. Our results indicate significant evolution in spiral arm properties over cosmic time. Specifically, the pitch angle decreases at a rate of 0.5 deg/Gyr (see also [82,83]) up to 11 Gyr (corresponding to $z \approx 2.5$), while the spiral-to-total ratio exhibits a slight increase with lookback time.

Overall, our findings in [60,64,65] demonstrate that the proposed model can successfully be applied to construct a broad range of spiral arm structures with diverse morphologies and across different wavelengths.

The numerous challenges in modeling spiral arms stem from the lack of a conclusive understanding of their nature, even within our own galaxy [84]. While advances in the quasi-stationary density wave theory [85–88] address the so-called “winding dilemma”, demonstrating this theory in N-body simulations remains challenging. The influence of bars [89,90] and tidal interactions caused by close flybys [91] can generate spiral patterns, but these structures may not be sustained over long periods. Alternatively, spiral arms may have a “dynamic” nature [92–94], co-rotating with the disk and forming through recurrent cycles of groove instabilities [95,96] or episodic stochastic star formation. A comprehensive review of these topics and competing theories can be found in [97–99].

Observations in IR bands provide valuable insights into the nature of spiral arms. Measurements in the near-infrared (NIR) bands can be used to estimate stellar mass and gravitational potential [76], while observations in the mid-infrared (MIR) filters serve as

reliable tracers of the star formation rate (SFR) [4,5,100,101]. FIR emission can also be used to measure the SFR and provides a means to estimate cold dust mass [102–105]. Under certain assumptions, dust mass estimates can be converted into gas mass fractions [38,42,43], offering further insights into the ISM properties of spiral galaxies.

To summarize, there are still plenty of questions about the dust—its distribution, mass, composition, and temperature on the galactic scale—and, from the dynamical perspective, we still face questions about the nature of large nonaxisymmetric features, such as spiral arms. At the same time, the proper photometric decomposition of resolved galaxies in several IR bands simultaneously could be quite beneficial for helping with these issues for the reasons listed above. In this paper, we decompose the images of three nearby spiral galaxies observed in the *Herschel* and *Spitzer* bands, covering a wavelength range from 3.6 μm to 250 μm . We model the classical bulge, bar, and disk components, along with the prominent spiral arms, using the previously developed sophisticated model [60,64,65]. The broad wavelength coverage enables us to (i) investigate the dust distribution in these galaxies, (ii) test for the presence of a density wave, and (iii) perform SED modeling of individual galactic components, estimating key properties such as dust mass (M_{dust}) and dust temperature (T_{dust}).

Our paper is organized as follows. In Section 2, we describe the sample selection process and the galaxies and images used in this study. Section 3 outlines the details of the decomposition process (Section 3.1) and the SED fitting with HerBIE (Section 3.2). In Section 4, we present the main results, including the light distribution analysis (Section 4.1), an evaluation of the nature of spiral arms (Section 4.2), and the dust properties of individual galactic components (Section 4.3). Finally, we summarize our findings in Section 5.

2. Data

As in our previous study of M51 [64], we use the DustPedia¹ [106] project as the primary data source. DustPedia, which is based on objects observed by the *Herschel* Space Observatory [107], is well suited for studying the role of dust in galaxies, making it an ideal fit for this work.

The database also includes a wide range of photometric data from other infrared surveys, such as the Two Micron All-Sky Survey (2MASS; [108]), the Wide-field Infrared Survey Explorer (WISE; [109]), the *Spitzer* Space Telescope [110], the InfraRed Astronomical Satellite (IRAS; [111]), and the *Planck* Observatory [112]. Additionally, DustPedia incorporates data from other parts of the spectrum, including the GALaxy Evolution eXplorer (GALEX; [113]), the Sloan Digital Sky Survey (SDSS; [114]), and the Digitized Sky Survey (DSS²), among others.

Images in all photometric bands have been carefully processed by [77], ensuring convenient and user-friendly access to the required data.

The multiwavelength catalog presented in DustPedia contains photometric data for 875 galaxies in the local Universe [77]. We visually selected galaxies from the catalog, choosing those that were not too small, not excessively inclined relative to the line of sight ($i < 70^\circ$), and exhibited clearly visible, prominent spiral arms. The preliminary sample, based on visual inspection, included 26 galaxies that display a variety of spiral patterns and angular sizes ranging from 2 arcmin to 20 arcmin. Three of these galaxies (NGC 4165, NGC 5364, and NGC 5427) were previously analyzed in a single 3.6 μm band in our earlier study [65]. Before proceeding with further analysis, all images were rotated to a “face-on” orientation with respect to the line of sight, using orientation parameters from [25] (Appendix D). Additionally, the sky background was subtracted where necessary.

The goal of this study is to analyze the distribution and properties of different types of dust (cold, warm, and hot) in galactic disks. To achieve this, we require the broadest possible

wavelength coverage from the NIR to the FIR. However, longer wavelengths result in lower spatial resolution and a larger point spread function (PSF) full width at half maximum (FWHM). Since we aim to investigate SEDs and reliably compare the properties of spiral structures in images obtained with different telescopes, all images must be processed to a uniform resolution and PSF. Consequently, the choice of the longest wavelength used influences the entire dataset. We adopt the SPIRE 250 μm band as the limiting wavelength for several reasons: (1) it provides an optimal balance between resolution and sensitivity; (2) for $\lambda > 250 \mu\text{m}$, image resolution rapidly deteriorates; and (3) it is close to the peak of cold dust emission, making it well suited for studying dust properties. For these reasons, we [64] and other researchers [45] have used SPIRE 250 μm as the limiting wavelength in similar studies.

In total, for each galaxy, we collected images in seven filters: 3.6 μm , 8 μm , 24 μm , 70 μm , 100 μm , 160 μm , and 250 μm . These images were obtained using the *Herschel* Space Observatory, with the Spectral and Photometric Imaging REceiver (SPIRE; [115]) and the Photodetector Array Camera and Spectrometer (PACS; [116]), as well as the *Spitzer* Space Telescope, using the InfraRed Array Camera (IRAC; [117]). The filters and their parameters are listed in Table 1. We chose to rely on Spitzer observations rather than those from WISE for constraining dust properties in our galaxy sample. The WISE W1 (3.4 μm) and W2 (4.6 μm) bands are either nearly equivalent to Spitzer IRAC1 (3.6 μm) and IRAC2 (4.5 μm) bands or do not intersect significantly with key PAH emission features, offering limited additional diagnostic value. Meanwhile, the W3 (12 μm) and W4 (22 μm) bands overlap with Spitzer MIPS coverage, but the Spitzer data provide superior sensitivity, resolution, and calibration. Additionally, the WISE W3 and W4 channels were affected by cryogenic limitations, especially after coolant depletion, which compromised data quality in these bands. Given these considerations, Spitzer data offer more reliable constraints on mid- and far-infrared dust emission.

Table 1. Infrared bands used in this work. Pixel size and PSF FWHM are given in arcseconds.

Name/Facility	λ , μm	Pixel Size	PSF FWHM	$\log_{10}(\lambda [\mu\text{m}])$
Spitzer 3.6 μm	3.6	0.75	1.66	0.56
Spitzer 8.0 μm	8.0	0.6	1.98	0.90
Spitzer 24 μm	24	1.5	6	1.38
PACS 70 μm	70	4	18	1.85
PACS 100 μm	100	3	10	2.00
PACS 160 μm	160	4	13	2.20
SPIRE 250 μm	250	6	18	2.40

Since we aim to construct SEDs and enable a robust comparison of parameters across individual morphological components, all images must be convolved to match the pixel scale and FWHM of the SPIRE 250 μm band, which are 6 arcsec and 18 arcsec, respectively. This convolution was performed using transition kernels from Aniano et al. [118] and the PSF matching tools from PHOTUTILS [119].

After the convolution step, approximately half of the galaxies in the preliminary sample appeared as too small and were excessively “blurred” by the PSF, making it difficult to distinguish individual features. Further selection among the remaining galaxies revealed several issues. In some cases, such as IC 342 and NGC 3031, the images were contaminated by bright galactic cirrus, which, despite its distinct color and geometric properties [120–122], is challenging to separate from the underlying galaxy. Additional complications arose due to framing issues (e.g., NGC 3184) or the presence of a nearby bright source (e.g., NGC 4725). Moreover, in a significant number of galaxies, the dust disk appeared as highly noisy, and the spiral arms were flocculent, as observed in NGC 5236,

NGC 5457, and NGC 6946. Since flocculent galaxies have many hardly resolved arms, constructing a reliable photometric model is either infeasible or requires substantial manual effort. As a result, we selected three galaxies from the initial sample—NGC 1097, NGC 1566, and NGC 3627—for which our photometric modeling appeared to be successful, as described in the following sections.

NGC 1097 is a strongly barred spiral galaxy, typically classified as SB(s)b, and located at a distance of 13–15 Mpc [123,124]. Morphologically, it features a pair of clearly defined spiral arms that converge into two prominent dust lanes extending along the bar for approximately 10 kpc. Additionally, its spiral structure exhibits visible tidal distortions associated with strong interactions with its companion galaxy, NGC 1097A, located to the northwest. Within the central region, at a radius of ~ 700 pc (8–10 arcsec), there is a ring of intense star formation [125,126], with a current SFR of $\sim 1.8 M_{\odot}/\text{yr}$ [127]. It is suggested that an instantaneous burst of star formation occurred inside the ring approximately 7 million years ago [128], leading to the formation of super star clusters visible in the optical range [129]. NGC 1097 also hosts an active galactic nucleus (AGN), exhibiting optical luminosity variations and transitioning between LINER 1 and Seyfert 1 classifications [130,131]. The nucleus contains a supermassive black hole (SMBH) with a mass of approximately $\sim 1.2 \times 10^8 M_{\odot}$ [132].

NGC 1566 is a barred spiral galaxy classified as SAB(s)bc and is the brightest member of the Dorado subgroup. It is so conspicuous in the southern celestial hemisphere that it has earned the nickname “The Spanish Dancer”. The distance estimates ranging from 6.5 Mpc to 17.8 Mpc according to different sources [123,133], and we adopt the latter since it was obtained with the more precise TRGB method. NGC 1566 is best known for its changing-look active galactic nucleus (CL AGN), which exhibits significant periodic flux variations across the optical, X-ray, and UV spectra [134,135], likely driven by nuclear disk instabilities [136]. The galaxy hosts an SMBH with an estimated mass of $\sim 10^7 M_{\odot}$ [137]. Some studies, however, suggest the presence of two merging SMBHs [138]. NGC 1566 features two remarkably prominent spiral arms that extend through multiple revolutions and are clearly visible in both the stellar and gaseous disks [139–141].

NGC 3627 (M 66) is classified as an SAB(s)b-type galaxy [142] with a prominent bar marked by luminous tips. It is a member of the Leo Triplet, which also includes NGC 3623 and NGC 3628. A strong tidal interaction is observed between NGC 3628 and NGC 3627, manifesting as an asymmetry in the gas and dust distribution, while NGC 3623 appears as largely unaffected [143,144]. NGC 3627 hosts a low-luminosity AGN of Seyfert 2 type [145]. Due to its distinct characteristics, it has been the focus of numerous studies, including but not limited to [146–148]. Additionally, NGC 3627 has hosted multiple recent supernovae, with at least three recorded in the past 30 years.

To conclude this section, the final sample consists of three late-type Sb galaxies: NGC 1097, NGC 1566, and NGC 3627. Their properties are listed in Table 2. In all cases, these galaxies exhibit at least two well-defined spiral arms in the IR bands, enabling their decomposition.

A strong bar is clearly visible in NGC 1097 and NGC 3627, while NGC 1566 also hosts a bar, though significantly smaller. Another common feature among these galaxies is that they all harbor AGNs and belong to galaxy groups. Additionally, all three are included in the PHANGS-ALMA observational program [149], which provides available spiral masks [73].

Despite these similarities, the galaxies represent fundamentally different cases in terms of dust distribution. According to the analysis by [25], their Sérsic profiles differ significantly: NGC 1097 has a very large Sérsic index ($n \gg 1$), NGC 1566 exhibits an intermediate value ($n \sim 1$), and NGC 3627 has a near-zero Sérsic index ($n \sim 0$).

These differences, illustrated in Figure 1, make these galaxies ideal candidates for testing more sophisticated decomposition models.

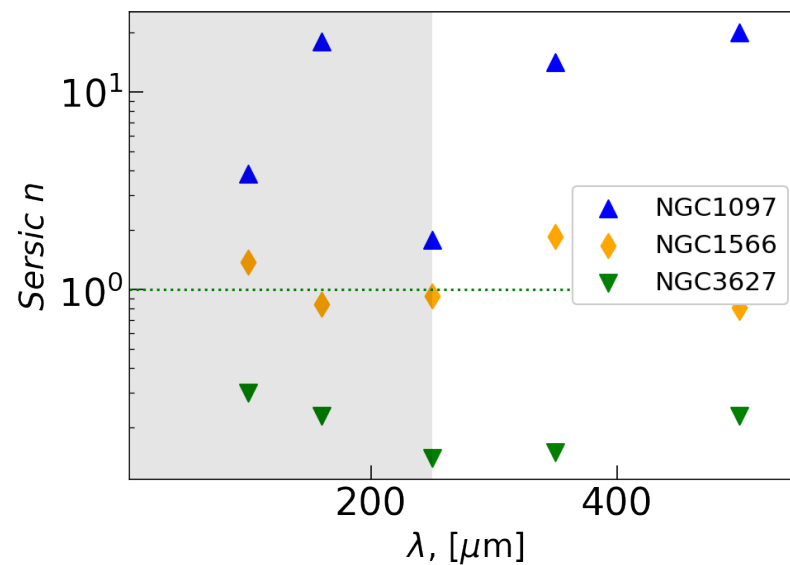


Figure 1. The Sérsic indices, n , for the galaxies under investigation, as reported by [25]. The light-gray-filled area marks the wavelength range studied in this work.

Table 2. Information about the galaxies in the sample, taken from [150]. Distances were obtained from the compilation in Table A2 of [123].

	NGC 1097	NGC 1566	NGC 3627
R.A. (J2000)	$2^h 46^m 19.12^s$	$4^h 20^m 00.42^s$	$11^h 20^m 15.02^s$
D.A. (J2000)	$-30^\circ 16' 30''$	$-54^\circ 56' 16''$	$+12^\circ 59' 30''$
Type	SBb	SABb	Sb
i	54.8°	49.1°	67.5°
P.A.	134°	44°	168°
Distance	13.6 ± 2.0 Mpc	17.7 ± 2.0 Mpc	11.3 ± 0.5 Mpc
Linear scale	394 pc/pix	513 pc/pix	501 pc/pix
$\langle B - V \rangle$	0.68 mag	0.57 mag	0.63 mag
B magnitude	9.69 mag	9.97 mag	9.09 mag
r_{25}	314 arcsec	217 arcsec	307 arcsec

3. Methodology

In this section, we provide a detailed description of the photometric decomposition process (Section 3.1) and the subsequent SED modeling of individual components (Section 3.2).

3.1. Decomposition

Before performing the decomposition, we applied a series of preparatory steps. The images in all bands, already convolved with the PSF, were cropped to an appropriate size to improve computational efficiency during the fitting process. For each image, we manually constructed a mask that covers foreground stars, neighboring galaxies, and other external objects, as well as any evident artifacts. In some cases, we also masked bright star-forming clumpy regions within the galaxy's structure, as these features cannot be accurately described by a smooth model and often cause the best-fitting spiral arms to deviate from their expected shape (see, for instance, the bright spot in Figure 2 for NGC 3627 in the southern region). Although it is theoretically possible to fit most of these clumps (see [151,152]), doing so is computationally challenging and will be considered in future work. During the

decomposition and χ^2 calculation, we utilized the error maps provided in the DustPedia archive, with a few exceptions where the original sigma maps were directly obtained from the IRSA database³.

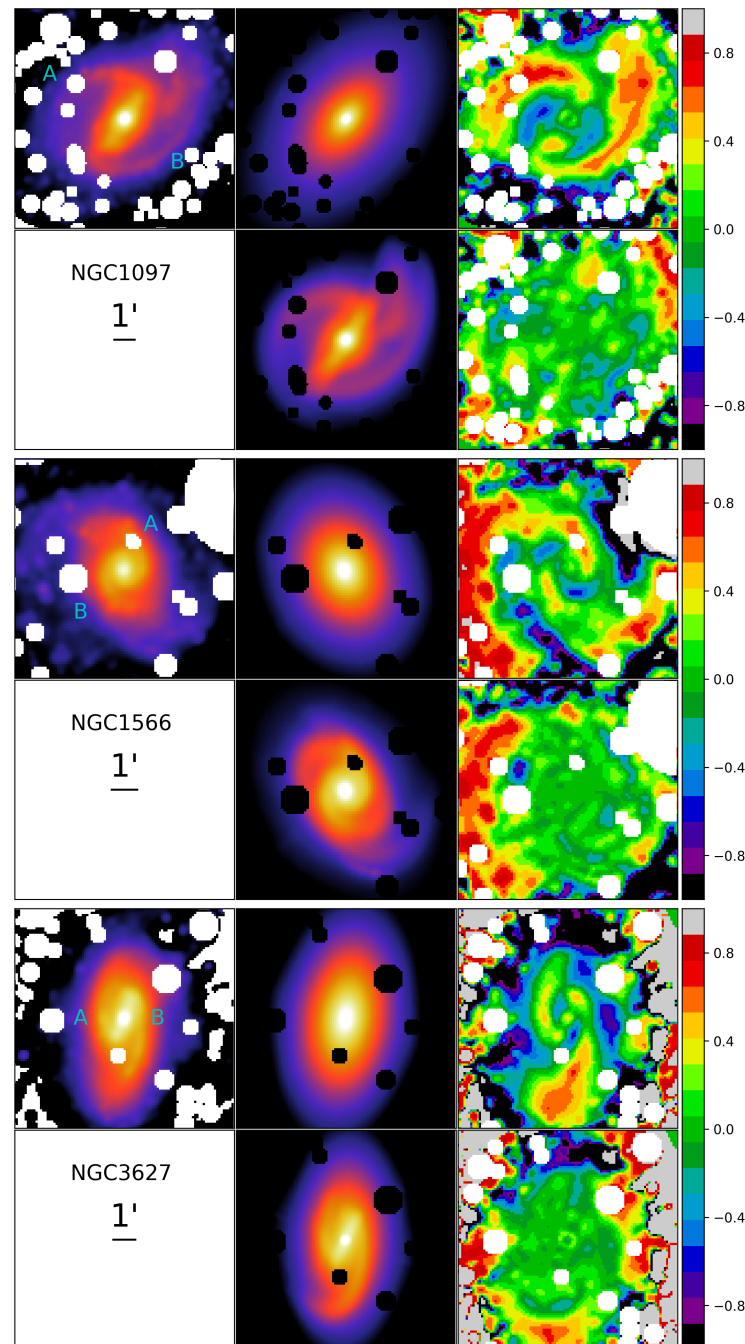


Figure 2. Photometric decomposition of the galaxies in the 3.6 μm band. The first row shows the original image (uppercase letters A/B mark individual spiral arms), the Sérsic-only model, and the corresponding relative residuals. The second row presents the full model and its relative residuals. The relative residual is defined as the difference between the original image and model fluxes, divided by the original image flux. The color bar on the right indicates the relative residual values, where colors close to green represent good agreement between the model and observations.

We utilized the IMFIT package [54] for photometric decomposition in this study. For each galaxy, we constructed two sets of models: (i) a single-component Sérsic model, following the approach of [25], and (ii) a multi-component model incorporating all relevant structural components. These included disks modeled with an exponential function [153],

bulges described by a Sérsic function [154], and bars modeled using a generalized ellipse function, implemented as `Sersic_GenEllipse`. Individual spiral arms were fitted using a specialized function detailed in [60] and implemented as an `IMFIT` class⁴.

Additionally, we modeled several of the brightest clumps and the unresolved AGN in NGC 3627 [130,131] as a `PointSource` component, which corresponds to the PSF scaled by a constant factor. The expected central depression in the galaxy, potentially caused by star formation suppression [155] or bar-induced effects, could also be incorporated into the model. However, since exponential disk models provided a satisfactory fit to the data, we did not introduce this modification.

The specific steps for fitting spiral arms are described in the next paragraph, while a detailed list of the components used for each galaxy is provided in Table 5.

In each of the three galaxies, we modeled two primary spiral arms, with some specific nuances. In NGC 1097, we additionally modeled a small segment visible in the upper-right corner. Unlike the other cases, both arms exhibit “breaks” in the model, forming a so-called pseudoring around the bar.

In NGC 1566, there is a noticeable sharp drop in the brightness of the spiral arms. To account for this, we modeled the inner and outer sections separately, labeling them as *in* and *out* where necessary. While NGC 1566 does contain a bar, it is relatively small (see, for example, the masks in [139]) and is nearly unresolved at the adopted resolution. Consequently, we did not include it in the model.

In NGC 3627, the left spiral arm (Spiral A) is better described by two distinct arms, which become particularly evident at the tips. Therefore, we included an additional faint arm model on the periphery, although our analysis focuses primarily on the bright inner arm, along with Spiral B. All spiral arms discussed in the following sections are labeled in Figure 2.

A crucial aspect of performing decomposition efficiently with such complex functions is selecting appropriate initial values. To achieve this, we utilized a script that recalculates parameters based on manually identified spiral arms in each image. These identifications rely on the original resolution as well as supplementary data from HST, JWST, and other sources, including HI observations [139,140].

The resulting models, presented in Figures 2 and A1–A3, provide a reasonable fit to the galaxies. Their properties are discussed in detail in Section 4.1; here, we briefly outline the key aspects that validate these models.

The first validation criterion is the visual appearance of the models. Similar to Figure 2 in [65], we present the models alongside the original images, along with relative residuals for the 3.6 μm band in Figure 2. As evident from these residual maps, even in challenging cases, the residuals remain small, primarily appearing in green. Additionally, the auxiliary Figures A1–A3, which display azimuthal profiles, demonstrate that the model effectively approximates both the individual “bumps” and the overall complex structure of the galaxies.

The second validation criterion comes from comparing the Sérsic-only models with previous measurements. The structural parameters obtained from these models are consistent with those measured in three filters in [25], supporting the reliability of our pipeline.

Following [64], we analyze the distribution of pixel values in the residual images and find them to be nearly symmetrical, with median values close to zero—an expected characteristic of well-constrained models. Furthermore, similar to [64], we assess whether the inclusion of a large number of additional parameters is justified. While increasing the model complexity naturally reduces χ^2 , we verify its justification using the Bayesian information criterion (BIC, [156,157]). The BIC is computed using a modified formula [158,159]:

$$\text{BIC} = \frac{\chi^2}{A_{\text{PSF}}} + k \cdot \ln \frac{n}{A_{\text{PSF}}}, \quad (1)$$

where A_{PSF} represents the number of pixels in the PSF, k is the number of free parameters, and n is the total number of pixels. In all cases, the BIC value is lower for the full model incorporating all components, validating its superiority over the oversimplified Sérsic-only version.

Although a full uncertainty estimation via a bootstrap resampling procedure in IMFIT is computationally expensive, we performed approximately ten iterations. The results confirm that the estimated parameters remain stable, reinforcing the robustness of the model.

Finally, an additional key validation comes from Figure 3, which shows that the total *modeled* SED aligns perfectly with the aperture-matched photometry from [77]. This agreement indicates that we have accounted for the majority of light sources accurately and comprehensively.

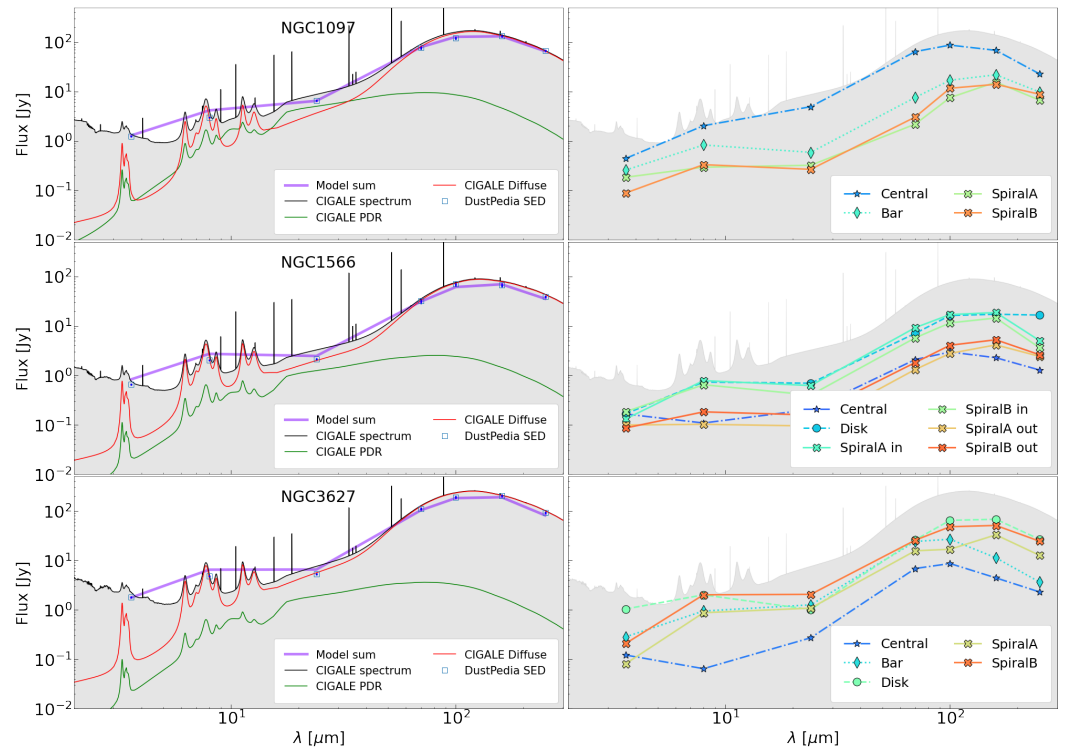


Figure 3. SEDs for the galaxies and their individual components. The left column presents the fits obtained by [21] using CIGALE with the THEMIS dust model. These fits include the total spectrum and separate contributions from photo-dissociation regions (PDRs) and diffuse dust, as well as the total flux sum for the components modeled in this work. The right column displays the total CIGALE fit alongside the SEDs for individual components in each galaxy.

3.2. SED Fitting with HerBIE

We performed component-wise dust SED fitting using the HerBIE (HiERarchical Bayesian Inference for dust Emission) model [49]. By employing a hierarchical Bayesian framework and the Markov chain Monte Carlo (MCMC) technique to infer dust parameters, this approach effectively mitigates certain inherent degeneracies among them. In previous studies, HerBIE has been successfully applied to both global and resolved SED fitting in large samples [38,160], as well as to individual objects [161–164].

As in previous studies, the fitting was performed under the assumption that grain properties follow the THEMIS model⁵, as presented in [50]. This framework does not intrinsically include polycyclic aromatic hydrocarbons (PAHs); instead, it models analogous small grains, which are partially hydrogenated amorphous carbons, denoted as a-C(:H). Additionally, THEMIS includes a population of a-C(:H)-coated large amorphous silicates and

large a-C(:H), with metallic inclusions. All dust grains are distributed by size according to the SED features that they exhibit in emission (see Figure 1 in [38]).

We modeled each component in every galaxy separately using all seven IR bands within the 3.6 μm –250 μm wavelength range, specifically, three bands from IRAC, three from PACS, and one from SPIRE. For each galaxy component, we used the flux estimates obtained during the decomposition process. Since IMFIT tends to underestimate uncertainties, we adopted the same relative errors for the individual components as those in the total SED. While this is a simplification, the obtained results show good agreement with independent sources, suggesting that the impact of this assumption is not critical. Another simplification is that all central components are modeled as the sum of the bulge and all other central structures, including the AGN. As demonstrated by [165–167], accurate radiative transfer modeling of the AGN requires additional assumptions about geometry and physical properties. While this is unlikely to significantly affect our results—since the AGN primarily heats dust outside the torus only in its immediate vicinity (see Figure 7 in [165])—all results related to the ‘Central’ components should nonetheless be interpreted with caution.

The results of the modeling are presented in Table 5, and the example of SED fitting is presented in Appendix B. For a detailed definition of the parameters derived by HerBIE, we refer the reader to Section 3.1 of [38]. Below, we provide a brief description of the key parameters: dust mass (M_{dust}), mean starlight intensity (\bar{U}), and the mass fraction of PAHs (q_{PAH}).

The dust mass M_{dust} is estimated under the assumption that it follows a power-law distribution of U and depends on the adopted distance (see Table 2). The starlight intensity U quantifies the interstellar radiation field (ISRF) that illuminates the dust grains. It is also related to the equilibrium temperature of large dust grains, assuming a Milky Way-like spectrum, via the relation $T_{\text{dust}} = 18.3[\text{K}] \times U^{(4+\beta)^{-1}}$, where the emissivity index is taken as $\beta = 1.7$ [21]. The THEMIS model does not include PAH, but has a population of small, stochastically heated aromatic-feature-carrying (AF) grains, which demonstrate similar properties. They can be used to estimate PAH mass fraction q_{PAH} following the relation from [38]: $q_{\text{PAH}} = 0.45 \times q_{\text{AF}}$. It is important to note that we perform this only in order to compare our results to the literature, and keep in mind that, in the discussion in Section 4.3, all mentions of q_{PAH} are actually derived from the amount of small a-C(:H).

4. Results and Discussion

In this section, we present the results of our analysis and discuss them in the context of previous studies.

4.1. Decomposition Results

In Figure 4, we present the fractional contributions of the different components in the modeled galaxies. Similar to the behavior observed for Sérsic indices, all three galaxies exhibit distinct structural characteristics.

For NGC 1097, we identify a highly luminous central region, consisting of a nuclear ring and an AGN, which accounts for more than half of the total light in most IR bands. Another notable feature is that, when spiral arms are included, the galaxy can be modeled with either a very small disk or, in some cases, no disk at all.

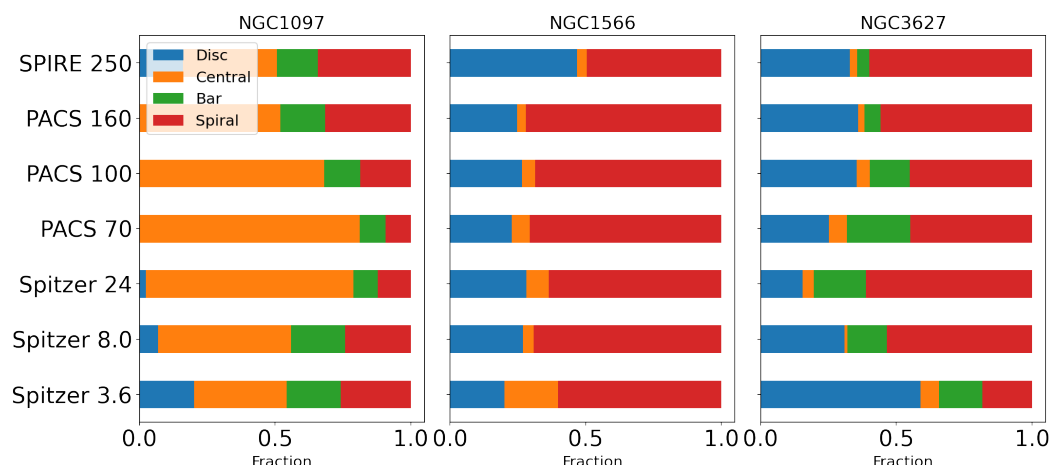


Figure 4. Fractions of the total light attributed to individual components, as measured in the photometric decomposition.

In NGC 1566, the spiral arms emerge as the most luminous component, which is expected given their prominence and extensive structure. In contrast, the fractional contribution of the spiral arms in NGC 3627 is lower. However, the bar and disk components are, on average, the most dominant among the sample.

In the following sections, we examine each galaxy in detail, with a particular focus on the ‘dust’ IR profile and its deviations from a standard exponential profile [25].

As evident from Figures 4 and A1, NGC 1097 has a significant fraction of its light concentrated in the central region. In all profiles, we observe a distinct “bump”, which is typically indicative of an early-type spiral galaxy with a prominent classical bulge [168]. However, in the case of NGC 1097, we know that the unresolved inner ring and the active nucleus also contribute significantly to the central brightness. As shown in Figure A1, this explains why the Sérsic-only profile exhibits an index of $n > 1$: it primarily captures the central structure and consequently deviates from the profile beyond 150–200 arcsec. In contrast, the full model accurately follows the profile across its entire extent, including the outer “bumps” produced by the spiral arms, which remain visible even after azimuthal averaging. The central component is well represented by a Sérsic profile with $n < 1$.

Another intriguing feature of NGC 1097 is its small or possibly absent dust disk. This arises from the fact that the signal level in the interarm regions, between the grand-design spiral pattern, is comparable to the noise level outside the galaxy in the same image. This effect is particularly evident in the PACS bands, where significant noise appears in the form of flocculent “filaments”, similar in structure to those found between the spiral arms. Notably, this characteristic is also present in the images at their original resolution. In principle, it is possible to model all other images of NGC 1097 without including the exponential disk component. The resulting models would exhibit only a slight degradation in terms of χ^2 and the BIC.

For NGC 1566, the situation is markedly different. The spiral arms are less pronounced and do not appear as distinct features in the surface brightness profiles, which overall exhibit a shape close to an exponential profile, as shown in Figure A2. Consistent with this observation, the Sérsic-only model yields an index of $n \approx 1$, in agreement with previous measurements by [25] and as illustrated in Figure 1. The galaxy is well represented by a model consisting of ‘classical components plus spiral arms’. Another interesting feature is that, in the azimuthal profile shown in Figure A2, the spiral arms collectively resemble an additional exponential disk. This effect may be a consequence of their considerable length and the number of full revolutions that they complete.

Finally, in the case of NGC 3627, we observe that the Sérsic index is close to zero in most bands. In other words, there is a central depression in the dust distribution, similar to what is found in approximately half of the galaxies analyzed in [25]. This behavior arises due to a ‘plateau’ extending from the center to the “bump” at ~ 70 arcsec, which forces a lower n value to achieve an optimal fit. This feature in the profile results from the significant contribution of both spiral arms, making NGC 3627 an example where the presence of spiral arms leads IR profiles to favor a Gaussian function over an exponential one. In fact, the possibility of such a profile for cold dust emission was previously discussed in Section 5.4.1 of [25] and in the case of M 81 by [169].

Before proceeding further, we highlight several similarities with previous studies. According to Figure 4, the spiral-to-total fraction (S/T) constitutes approximately 20–60% of the total light, which is consistent with the estimates from [63–65]. Moreover, [65] found (see Figure 8 in their work) that, in the 3.6 μm Spitzer band, the S/T ratio reaches its maximum for galaxies with Hubble types $T \approx 3\text{--}5$. This trend is also observed in our study, except when considering the central components of NGC 1097.

The parameters for the spiral arms are listed in Table 3. Similar to the multiwavelength analysis of M 51 conducted by [64], we find that the width of the spiral arms is smallest in the 24–70 μm range. This can be connected with the fact that spiral arms in these bands are associated with ongoing star formation, which cannot propagate far enough from the place of birth [170]. Additionally, the pitch angle remains roughly constant across wavelengths, though its variation along the arm is significant (see also [171]). This aspect is further discussed in Section 4.2.

Table 3. Measured parameters for the models of individual spiral arms.

Galaxy/Spiral	Band	Spiral/Total	Pitch ψ , Deg	Width, Arcsec
NGC 1097 A	Spitzer 3.6	0.14	17.88 ± 1.82	69.92 ± 0.69
NGC 1097 A	Spitzer 8.0	0.07	13.89 ± 1.06	24.07 ± 1.43
NGC 1097 A	Spitzer 24	0.05	14.11 ± 1.07	30.27 ± 3.15
NGC 1097 A	PACS 70	0.03	13.58 ± 1.24	20.18 ± 0.32
NGC 1097 A	PACS 100	0.06	12.70 ± 1.42	27.91 ± 0.33
NGC 1097 A	PACS 160	0.12	14.37 ± 1.21	33.83 ± 0.44
NGC 1097 A	SPIRE 250	0.10	13.59 ± 1.10	22.26 ± 0.85
NGC 1097 B	Spitzer 3.6	0.07	18.25 ± 1.67	50.86 ± 0.68
NGC 1097 B	Spitzer 8.0	0.08	20.51 ± 0.45	33.33 ± 1.08
NGC 1097 B	Spitzer 24	0.04	21.34 ± 0.32	51.25 ± 4.72
NGC 1097 B	PACS 70	0.04	17.70 ± 0.58	51.78 ± 0.00
NGC 1097 B	PACS 100	0.09	22.05 ± 1.75	58.90 ± 0.00
NGC 1097 B	PACS 160	0.11	20.94 ± 0.43	45.92 ± 0.49
NGC 1097 B	SPIRE 250	0.13	18.13 ± 0.78	31.47 ± 0.78
NGC 1566 A _{in}	Spitzer 3.6	0.16	27.79 ± 2.70	47.03 ± 1.30
NGC 1566 A _{in}	Spitzer 8.0	0.29	19.93 ± 5.96	34.21 ± 0.65
NGC 1566 A _{in}	Spitzer 24	0.25	30.17 ± 3.92	39.12 ± 2.36
NGC 1566 A _{in}	PACS 70	0.30	24.75 ± 4.84	29.82 ± 0.00
NGC 1566 A _{in}	PACS 100	0.28	24.75 ± 4.84	33.22 ± 0.00
NGC 1566 A _{in}	PACS 160	0.27	24.75 ± 4.84	39.80 ± 0.63
NGC 1566 A _{in}	SPIRE 250	0.14	21.99 ± 3.92	14.87 ± 2.37
NGC 1566 B _{in}	Spitzer 3.6	0.22	13.97 ± 7.34	58.32 ± 0.00
NGC 1566 B _{in}	Spitzer 8.0	0.24	11.16 ± 15.63	42.22 ± 0.97
NGC 1566 B _{in}	Spitzer 24	0.16	29.56 ± 2.89	34.62 ± 2.96
NGC 1566 B _{in}	PACS 70	0.18	26.80 ± 5.13	30.34 ± 0.00
NGC 1566 B _{in}	PACS 100	0.19	26.80 ± 5.13	33.79 ± 0.00
NGC 1566 B _{in}	PACS 160	0.21	26.80 ± 5.13	42.95 ± 0.00

Table 3. Cont.

Galaxy/Spiral	Band	Spiral/Total	Pitch ψ , Deg	Width, Arcsec
NGC 1566 B _{in}	SPIRE 250	0.10	25.13 ± 2.64	12.16 ± 2.26
NGC 1566 A _{out}	Spitzer 3.6	0.12	14.34 ± 0.50	58.41 ± 0.00
NGC 1566 A _{out}	Spitzer 8.0	0.04	18.54 ± 0.60	36.21 ± 2.98
NGC 1566 A _{out}	Spitzer 24	0.04	17.68 ± 0.38	38.39 ± 0.00
NGC 1566 A _{out}	PACS 70	0.04	17.23 ± 0.32	28.35 ± 0.00
NGC 1566 A _{out}	PACS 100	0.05	17.23 ± 0.32	31.58 ± 0.00
NGC 1566 A _{out}	PACS 160	0.06	17.23 ± 0.32	40.14 ± 0.00
NGC 1566 A _{out}	SPIRE 250	0.07	18.54 ± 0.86	44.39 ± 6.31
NGC 1566 B _{out}	Spitzer 3.6	0.10	10.88 ± 0.00	57.63 ± 0.00
NGC 1566 B _{out}	Spitzer 8.0	0.07	12.15 ± 0.00	42.61 ± 0.00
NGC 1566 B _{out}	Spitzer 24	0.06	23.69 ± 0.00	39.94 ± 0.00
NGC 1566 B _{out}	PACS 70	0.06	11.89 ± 0.00	27.67 ± 0.00
NGC 1566 B _{out}	PACS 100	0.07	11.89 ± 0.00	30.83 ± 0.00
NGC 1566 B _{out}	PACS 160	0.08	11.89 ± 0.00	39.18 ± 0.00
NGC 1566 B _{out}	SPIRE 250	0.07	14.80 ± 0.00	37.56 ± 4.68
NGC 3627 A	Spitzer 3.6	0.07	18.23 ± 1.54	54.96 ± 0.00
NGC 3627 A	Spitzer 8.0	0.22	17.17 ± 0.94	16.46 ± 0.02
NGC 3627 A	Spitzer 24	0.30	26.26 ± 0.50	23.39 ± 11.56
NGC 3627 A	PACS 70	0.20	27.09 ± 0.17	13.08 ± 0.45
NGC 3627 A	PACS 100	0.19	19.57 ± 0.30	16.15 ± 1.21
NGC 3627 A	PACS 160	0.29	14.14 ± 1.73	29.91 ± 0.71
NGC 3627 A	SPIRE 250	0.30	11.76 ± 2.20	25.06 ± 1.36
NGC 3627 B	Spitzer 3.6	0.12	22.35 ± 0.25	56.44 ± 0.00
NGC 3627 B	Spitzer 8.0	0.31	13.75 ± 0.30	29.02 ± 0.01
NGC 3627 B	Spitzer 24	0.31	17.45 ± 0.06	23.87 ± 3.79
NGC 3627 B	PACS 70	0.25	16.83 ± 0.05	23.15 ± 0.23
NGC 3627 B	PACS 100	0.26	15.01 ± 0.22	26.28 ± 0.39
NGC 3627 B	PACS 160	0.27	20.30 ± 0.18	29.00 ± 0.41
NGC 3627 B	SPIRE 250	0.30	18.55 ± 0.26	24.60 ± 0.78

4.2. Presence of Density Wave

Measurements of the properties of spiral arms can provide insights into the nature of spiral structure in galaxies. The general concept is that, if a galaxy exhibits a long-lived density wave (DW) rotating with a constant pattern angular velocity, Ω_p , then the pattern rotates faster than the disk at large distances from the center and more slowly than the disk in the inner regions. This behavior produces an observable effect: beyond the so-called corotation radius (CR), where the disk and spiral pattern angular velocities are equal, newly formed stars may appear to move downstream relative to the main population of older stars. If the galaxy's rotation curve is known, estimating the CR is equivalent to determining the corresponding pattern speed, Ω_p .

Based on this fundamental idea, various observational methods have been employed to determine the CR. These include measuring the skewness of the intensity profile along the spiral arm [172], analyzing color gradients along the arm [173], and identifying offsets between young star clusters and their nearest H II regions [174], among other techniques. However, the most common approach involves comparing the pitch angle, ψ , in different wavelength bands. The general consensus is that the pitch angle in redder bands, which trace the older stellar population, should be larger than in bluer bands, which are associated with ongoing star formation [175]. However, it is important to note that this simplified picture can be more complex due to additional physical processes [78,176].

As noted by [171], spiral arms can adopt various shapes [177] (see also Chugunov et al., in prep.). Therefore, it is important to emphasize that our measurements account for the

total distribution of light across the spiral arms. As a tracer of the old stellar population, we use the Spitzer 3.6 μm band. For indicators associated with star formation, we use MIR images in the 8 μm , 24 μm , and 70 μm bands, where warm dust is believed to be heated by UV photons from young stars [4,100]. The total FIR emission is also commonly used as such an indicator [5,102]. However, since we do not analyze wavelengths beyond 250 μm due to low resolution, we do not include it in our study.

According to the data in Table 3, we find no galaxy in which the pitch angle, ψ , at 3.6 μm is consistently larger than in any of the star-formation-related indicators for both arms. Given the substantial variation in the pitch angle, we also estimate it over the entire extent of each arm and arrive at the same conclusion.

This result can be interpreted as evidence against the presence of a stationary density wave in these galaxies. Additional arguments supporting this interpretation, along with comparisons to previous studies, are presented below. However, before addressing these points, we first assess whether this effect can be detected in principle, given the resolution limitations of our data. To investigate this, we follow the approach of [64]. Assuming a flat rotation curve, $v(R) = v_0$, a pitch angle ψ in one indicator, and a time delay Δt corresponding to the time a star takes to cross the arm and evolve [100], we can determine the modified pitch angle, ψ' , for a second indicator using the following formula:

$$\psi' = \arctan\left(\frac{1}{\tan \psi} \pm \frac{\Omega \times (1 - \beta)}{\log \beta} \times \Delta t\right)^{-1}$$

where $\beta = R_{\text{out}}/R_{\text{CR}}$ is the ratio of the arm length to the corotation distance, and $\Omega = v_0/R_{\text{out}}$. The \pm sign indicates that the azimuthal offset can occur in either direction. For the plateau values of the rotation curve, v_0 , we adopt 250 km/s for NGC 1097 [178], 180 km/s for NGC 1566 [179], and 200 km/s for NGC 3627 [180]. Using the pitch angles and arm extensions from Table 3, assuming that the CR is located at the midpoint of the arm and using $\Delta t = 5/10/20/50/100$ Myr, we estimate the difference $\Delta\psi = |\psi - \psi'|$. We find that, for NGC 1566 and NGC 3627, the average $\Delta\psi \approx 5^\circ$ for $\Delta t = 10$ Myr, which should be detectable for all time intervals equal to or greater than this. For NGC 1097, we measure $\Delta\psi \approx 3^\circ$ for $\Delta t = 20$ Myr. While the effect in this galaxy is smaller, the well-constrained shape of the spiral arms suggests that this offset should still be detectable.

Another related method, which is in fact more direct and can also be applied in this study, involves measuring the precise angular offsets between the same two indicators. As demonstrated by [100,181], in the case of a density wave, these offsets should follow the following:

$$\Delta\phi(R) = (\Omega(R) - \Omega_p) \times \Delta t, \quad (2)$$

where $\Omega(R)$ and Ω_p are the angular velocities of the disk and the spiral pattern, respectively, and Δt represents the time interval between two evolutionary stages of the stellar population. If the rotation curve is known—which is available for all three galaxies from [178–180]—we can derive the exact form of the angular offset profile and estimate the location of the CR at the point where the offset crosses zero, $\Delta\phi(R) = 0$. This method has been shown to be effective and generally consistent with other approaches (see [182]), though it has certain limitations [181]. However, these shortcomings can be mitigated by incorporating the full light distribution for proper modeling. We measure these angular offsets using the same indicators as those employed for the pitch angle analysis. For nearly all spiral arms, we observe a consistent pattern: the offset is oriented in one direction, with the 3.6 μm band tracing the outer convex part of the arm, while the star-formation-related images occupy the inner concave region. The only exceptions are Spiral A_{out} in NGC 1566, where we detect a zero-crossing that does not align with the expected rotation curve,

and Spiral A_{in} in NGC 1566, where the indicators appear to switch positions. However, in this case, the offsets are too small to be reliably distinguished. This observed behavior is consistent with certain tidal interaction scenarios, where kinematic spiral arms rotate with a lagging pattern speed, $\Omega_p = \Omega(R) - \kappa/2$, where κ is the epicyclic frequency ([183] and references therein). Under this model, we expect to observe similar pitch angles and unidirectional offsets, as seen in our measurements.

Additionally, we highlight other arguments that support our results. Ref. [184] found that measurements of the CR estimated using different methods often show significant discrepancies. In Table 4, we list various CR measurements collected from the literature. Most of these data points were obtained using the only direct method proposed by Tremaine and Weinberg [185].

Table 4. Corotation parameters from [184] and other sources. The method acronyms are as follows: ‘P-D’ refers to the azimuthal profile phase method; ‘T-W’ represents the Tremaine–Weinberg method [185]; ‘offset’ corresponds to methods similar to those discussed in Section 4.2; ‘morph’ denotes symmetry-related methods; ‘F-B’ refers to the velocity phase reversal method [186]; ‘model’ includes various modeling approaches; ‘torque’ estimates gravitational torques exerted by the potential on the gas [187]. Further details can be found in the referenced papers. Note that some CR measurements apply to the bar and are included in cases where the spiral pattern exhibits the same pattern speed.

Galaxy	#	CR, Arcsec	Method	Ref.
NGC 1097	1	96.60 ± 30.5	T-W	[188]
...	2	234.3 ± 8.1	morph	[189]
...	3	142.8 ± 0.0	model	[190]
...	4	114.5 ± 7.1	F-B	[191]
...	5	122.7 ± 7.1	model	[192]
...	6	97.5 ± 12.2	torque	[193]
NGC 1566	1	44.40 ± 26.64	T-W	[188]
...	2	78.78 ± 31.8	T-W	[188]
...	3	46.98 ± 29.22	T-W	[188]
...	4	98.70 ± 5.1	morph	[189]
...	5	97.20 ± 4.1	P-D	[194]
...	6	122.17 ± 45.45	offset	[195]
...	7	127.39 ± 36.38	offset	[195]
...	8	72.57 ± 7.0	torque	[193]
NGC 3627	1	34.64 ± 1.46	T-W	[188]
...	2	77.08 ± 26.34	T-W	[188]
...	3	85.86 ± 8.78	T-W	[188]
...	4	94.64 ± 55.62	T-W	[188]
...	5	171.00 ± 28.5	offset	[100]
...	6	163.00 ± 0.0	T-W	[196]
...	7	95.0 ± 3.7	torque	[193]

For NGC 1097, we only have two CR measurements; however, a similar situation is observed across all galaxies: the estimated corotation radii are scattered throughout the disk without a clear consensus, and their uncertainties encompass either the entire disk or a significant fraction of it (see images in the [184] repository).

If we assume a single CR—which is not necessarily the case [197]—such disagreement may indicate the dynamic nature of the spiral arms (as suggested for NGC 4321 in [182]). Alternatively, other explanations may exist, but the observed discrepancies do not support the presence of a well-defined and strong stationary density wave.

Ref. [198] investigated global spiral modes in NGC 1566 and found that the disk is stable against spiral perturbations under a linear stability analysis framework.

Additionally, we performed a simple test using the manual slicing technique described in [63]. The objective was to fact-check the position of the spiral arms using a more traditional star formation tracer, namely the GALEX FUV image, which could potentially reveal a clearer offset signal. We measured similar pitch angles in the GALEX FUV band as those obtained previously, as well as in the Spitzer 3.6 μm band, where we also applied the slicing technique. Across all seven measured arms (with only one studied in NGC 3627), we found $\psi_{3.6} \leq \psi_{FUV}$, which we interpret as further confirmation of our results. The study in [175] measured pitch angles for approximately 80 galaxies, including NGC 1097 and NGC 1566, using both one-dimensional and two-dimensional Fourier transformation methods. Their analysis covered a wide range of wavebands, namely 3.6 μm , IRVB, NUV, and FUV, detecting a mild decrease in pitch angle from the reddest to the bluest bands in general. However, in the two galaxies examined here, no such trend was observed (see Table 1 in [175]), except in the 1D method for NGC 1097. In this case, a very narrow radial range (120–181 arcsec) was used, making the result less reliable.

Finally, all three galaxies reside in galaxy groups and exhibit signs of tidal interactions. Collectively, this evidence may suggest a tidal origin for the spiral patterns in NGC 1097, NGC 1566, and NGC 3627.

4.3. SED Fitting Results

The dust properties of individual components are presented in Table 5. Before proceeding with further discussion, we note that resolved dust SED fitting has been performed in previous studies [43,44], though typically on relatively small samples. One exception is the recent work by [42], in which the authors estimated the SED for approximately 800 nearby galaxies, including NGC 3627 and NGC 1566, over the same wavelength range of 3.6 μm –250 μm . However, even when a resolved SED is available for a given object, the component-wise fitting approach applied in this study remains valuable due to several advantages: (i) the number of fitted distributions is significantly smaller, making it easier to control the quality of the fit; (ii) to derive information about the properties of individual components, they must still be separated from one another.

All three galaxies analyzed in this study are late-type systems with $T \approx 3\text{--}4$ and thus contain significant amounts of dust and gas, placing them near the peak of the distribution among Hubble stages (see Figure 6 in [21]). As evident from Table 5, the largest fraction of large-grain dust is contained within the disk. However, the spiral arms also contribute a substantial portion of the total dust mass, M_{dust} , with each arm containing approximately $10^6\text{--}10^{6.5} M_{\odot}$ ($\sim 10\%$ of the total dust mass in NGC 1097 and NGC 1566, and $\sim 20\%$ in NGC 3627). This dust is distributed over a more compact area, leading to enhanced spiral arm contrast (see, e.g., [30,163,199]). The total dust mass, M_{dust} , obtained by summing the contributions from individual components is in good agreement with the estimate from [21] for NGC 1566. However, for NGC 1097, our estimate is systematically higher, whereas, for NGC 3627, it is lower by the same 0.3 dex. All values have been corrected for distance. This discrepancy may arise from uncertainties, residual unaccounted light, differences in background subtraction, or the so-called “Matryoshka effect”, which highlights the impact of spatial resolution on constrained dust parameters [49]. Nevertheless, the discrepancy between the M_{dust} estimates from [21,42] is even larger, suggesting that our results remain within the expected accuracy of SED fitting. Furthermore, the estimates from [200] for NGC 1097 and NGC 3627 are in close agreement with those from [21].

Regarding PAHs, we note several key findings. The first and most evident result is that q_{PAH} is lower in the central regions, as indicated by SED fitting. This behavior

is expected, as PAH formation via shattering is inefficient in these environments, while depletion through coagulation is significant [163,201].

The second finding is somewhat surprising: in all three galaxies, the average fraction of these small grains is similar in both the disk and the spiral arms. This result is confirmed by the maps from [42], where the spiral arms exhibit little contrast, except in the densest star-forming regions, where q_{PAH} is lower. Furthermore, these maps reveal a gradual increase in the PAH fraction toward the periphery of the disk, reaching approximately 8%. Similar results were obtained for NGC 3627 by [43]. Indeed, PAH emission remains strong in interarm regions, contributing up to 90% of the total MIR emission, as observed in M83 [74]. PAHs are expected to be efficiently destroyed in H II regions, which are abundant in spiral arms [202]. However, it is also possible that the total IR emission is not dominated by H II regions, as photodissociation regions (PDRs) are also numerous in spiral arms. The SED of H II regions can, to some extent, be modeled with a hot modified black-body (MBB) model [21] at approximately 30 K. These regions contribute to the MIR continuum between 20 μm and 60 μm but, overall, the dust mass from the neutral medium (constrained in the fitting by far-IR emission) and the PAH fraction (controlled by the 8 μm window) are not significantly affected by the presence of H II regions. For the inner bright regions of the spiral arms in NGC 1566, we observe a noticeable increase in q_{PAH} . However, the arm-averaged value remains close to that of the disk. Additionally, the finding that q_{PAH} is similar between the disk and spiral arms in all three galaxies may be due to the fact that, on large scales, PAH abundance is primarily regulated by metallicity. According to [13], at solar metallicity, we indeed expect $\ln(q_{\text{AF}}) \approx -1.7$.

In NGC 3627, the bar is visibly deficient in PAHs, likely due to strong dust heating at its tips, which is also evident in the maps from [42]. This feature is common in barred galaxies [22].

The dust temperature, evaluated from the interstellar radiation field (ISRF) parameter \bar{U} , indicates that dust in the spiral arms is relatively cold, with $T_{\text{dust}} \approx 18\text{--}20$ K. This trend is also evident from the SEDs in Figure 3, where the peak of FIR emission for each spiral arm is shifted to longer wavelengths compared to the total fit. Additionally, Figure 4 demonstrates that the fractional contribution of spiral arms increases in bands where dust is colder.

For NGC 1566, we observe a temperature gradient, with an inner dust temperature of approximately 25 K decreasing by ~ 5 K toward the periphery. In NGC 3627, the overall decrease in T_{dust} from the center outward is consistent with the spatially resolved SED fitting results reported by [43] (see their Figure 10). Furthermore, based on the fits from [21], it is evident that, in each case, the dust contained within the spiral arms is systematically colder than the average dust temperature in the galaxy.

The connection between dust properties and the nature of spiral patterns remains poorly understood. Only a few models that explore this relationship exist [203,204], primarily linking dust properties to the corotation radius and the presence of dust lanes on one side of the spiral arms. In our own galaxy, observations indicate that the spiral pattern sorts dust by size and fragments it in such a way that different types of grains accumulate on opposite edges of the spiral arms [205].

Other studies suggest that the distribution of supernovae, which play a role in regulating dust content, may also be influenced by the spiral pattern [206]. This is particularly relevant for NGC 1566, which has hosted an exceptionally high number of supernovae, though the full implications of this remain under debate. Another avenue of investigation is whether star formation in spiral arms is enhanced due to the velocity gradient induced by the density wave, which could be examined by measuring the arm-to-interarm contrast [73].

The dust-to-gas mass ratio (D/G) can be estimated from metallicity. For these three galaxies, $12 + \log(\text{O}/\text{H}) \approx 8.55$ [21], implying a D/G ratio of several $\times 10^{-3}$ [38]. This value could be compared with the star formation rate contrast to determine whether star formation is enhanced in the spiral arms [207]. In principle, this hypothesis could be tested in future studies with a larger sample of galaxies.

Table 5. Dust parameters of individual components derived from HerBIE SED fitting. A description of the individual parameters is provided in the last paragraph of Section 3.2. All values are expressed in natural logarithm, except for the total dust mass, which is given in decimal logarithm, with Δ representing the uncertainty. For the total values of each galaxy, the temperature data are taken from [21], while other parameters are from [38]. For comparison, the last column shows sum of dust mass estimates in this work (decimal logarithm) and fraction of each component. Dust masses have been corrected for the distances listed in Table 2.

Component	$\ln q_{\text{AF}}$	Δ	T_{dust}	Δ	$\log M_{\text{dust}}$	Δ	Total
NGC1097	−2.33	0.02	24.47	0.69	7.71	0.02	7.42
Central	−2.52	0.11	27.63	1.68	6.51	0.15	12%
Bar	−1.65	0.09	21.42	0.81	6.39	0.09	9%
Disk	−1.99	0.14	13.35	1.45	7.18	0.23	57%
Spiral A	−1.95	0.10	18.43	0.51	6.42	0.07	10%
Spiral B	−2.01	0.10	18.78	0.63	6.48	0.08	11%
NGC1566	−2.19	0.12	22.76	0.98	7.68	0.03	7.55
Central	−2.51	0.17	22.09	2.12	5.85	0.23	2%
Disk	−1.78	0.11	15.31	1.42	7.48	0.22	84%
Spiral A _{in}	−1.62	0.11	26.11	0.98	6.10	0.08	4%
Spiral B _{in}	−1.47	0.10	25.49	0.82	6.00	0.07	3%
Spiral A _{out}	−1.78	0.11	20.74	1.06	6.08	0.12	3%
Spiral B _{out}	−2.17	0.13	18.76	1.22	6.19	0.16	4%
NGC3627	−2.86	0.06	24.62	0.67	7.53	0.03	7.07
Central	−4.11	0.24	26.14	2.66	5.39	0.24	2%
Bar	−2.12	0.12	36.47	1.11	5.15	0.06	1%
Disk	−1.93	0.10	22.74	0.57	6.55	0.06	30%
Spiral A	−1.85	0.11	19.50	1.45	6.60	0.18	34%
Spiral B	−1.73	0.10	22.30	1.14	6.58	0.12	32%

5. Conclusions

For the three late-type spiral galaxies under investigation—NGC 1097, NGC 1566, and NGC 3627—we have obtained images from DustPedia [77] in seven infrared (IR) bands (3.6, 8, 24, 70, 100, 160, and 250 μm). We performed photometric decomposition using two types of models: the Sérsic profile, as previously applied in [25], and a full multicomponent model. The latter includes the explicit modeling of spiral arms, utilizing our previously developed method introduced in [65].

Consistent with our earlier studies of M 51 [64] and HST/JWST data [60], we confirm that the model that we developed can be effectively applied to analyze images across a broad range of wavelengths. Our findings include the following:

- The parameters of the spiral arms in the IR bands are similar to those obtained earlier for M 51 and other galaxies. Specifically, the spiral contribution to total luminosity ranges from 20% to 60%, increasing in the FIR bands. The width of the arms is minimal at 24–70 μm .
- Regarding dust distribution, we find that, in all cases, the emission profile is well described by an exponential disk, provided that non-axisymmetric components such

as spiral arms and bars are properly accounted for. This effect is most evident in NGC 3627, where the atypical dust distribution profile (Sérsic index $n \sim 0$) results from a bump induced by the influence of spiral arms. For NGC 1097, the large Sérsic index ($n \gg 1$) is attributed to the presence of a bright AGN and a nuclear ring. Although these three cases do not fully resolve the question of the central dust depletion raised in [25], they illustrate how careful modeling in late-type galaxies can address this issue.

- (iii) By utilizing bands associated with old stars (which trace the gravitational potential) and recent star formation, and considering the full light distribution along the spiral arms, we tested the predictions of the stationary density wave theory. The measured pitch angles are approximately 20° , and the angles in different wavelengths do not reveal expected inequalities, and thus do not support the presence of a stationary density wave. Furthermore, the angular offsets between individual tracers also fail to align with this theory. Given the presence of companion galaxies in all cases, it is more likely that the spiral arms have a dynamic or tidal origin rather than being driven by a stationary density wave.
- (iv) We performed SED fitting in the wavelength range of $3.6 \mu\text{m}$ to $250 \mu\text{m}$ for individual galaxy components, including spiral arms, which has not been performed in this manner before. Our results indicate that the average PAH fraction (q_{PAH}) is nearly identical in the disk and spiral arms. Additionally, spiral arms contain a significant (10–60%) fraction of the total dust in galaxies, with an estimated dust temperature (T_{dust}) of approximately 18–20 K, indicating that the dust is predominantly cold. Furthermore, we observe evidence of a dust temperature gradient in NGC 1566, where the separate modeling of the inner and outer spiral arms revealed a systematic variation in T_{dust} .

These results underscore the importance of incorporating spiral arms into photometric decomposition and the critical role that they play in addressing key questions about galaxy evolution. This pilot study serves as a foundation for future research and will be expanded to a larger sample of galaxies as additional observations become available.

Author Contributions: Conceptualization, A.A.M. and I.V.C.; methodology, A.A.M., F.G., V.S.K., and I.V.C.; validation, A.A.M., I.V.C., F.G., and V.S.K.; investigation, A.A.M., V.S.K., and P.V.S.; data curation, A.A.M. and P.V.S.; writing—original draft preparation, A.A.M.; writing—review and editing, A.A.M., A.V.M., I.V.C., G.A.G., V.B.I., S.S.S., A.A.S., and D.M.P.; visualization, A.A.M. and I.V.C. All authors have read and agreed to the published version of the manuscript.

Funding: We acknowledge financial support from the Russian Science Foundation, grant no. 20-72-10052.

Data Availability Statement: The data underlying this article will be shared upon reasonable request to the corresponding author.

Acknowledgments: DustPedia is a collaborative focused research project supported by the European Union under the Seventh Framework Programme (2007-2013) call (proposal no. 606847). The participating institutions are Cardiff University, UK; National Observatory of Athens, Greece; Ghent University, Belgium; Université Paris Sud, France; National Institute for Astrophysics, Italy and CEA, France.

Conflicts of Interest: The authors declare no conflicts of interest.

Abbreviations

The following abbreviations are used in this manuscript:

SED	Spectral energy distribution
BIC	Bayesian information criterion
CR	Corotation radius
PSF	Point spread function
FWHM	Full width at half maximum
SPIRE	Spectral and Photometric Imaging REceiver
PACS	Photodetector Array Camera and Spectrometer
IRAC	InfraRed Array Camera
NIR	Near-infrared
MIR	Mid-infrared
FIR	Far-infrared

Appendix A. Models for All Bands

This appendix presents data and models for six bands in the 8–250 μm range, shown in Figures A1–A3. Models for the Spitzer 3.6 μm images are displayed in Figure 2. To optimize space and provide an alternative perspective, we present azimuthally averaged profiles.

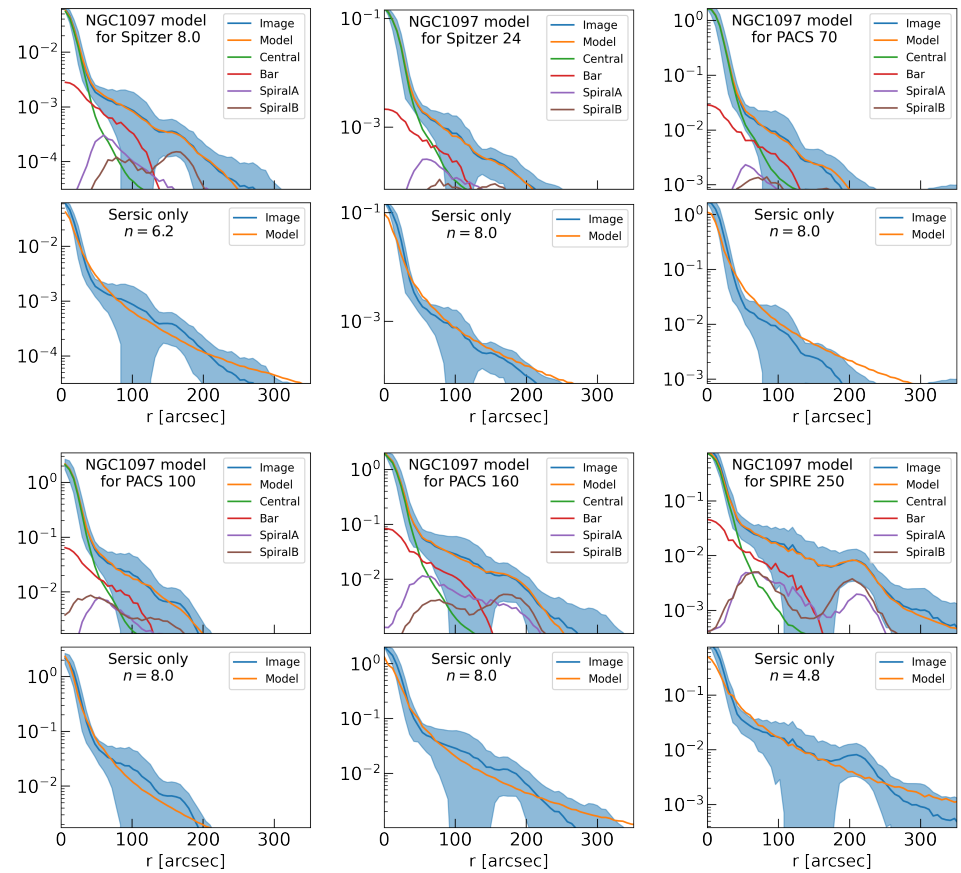


Figure A1. Azimuthally averaged profiles for the NGC 1097 model and data in all bands except 3.6 μm , which is presented in Figure 2. In each pair of images, the full model is shown above the Sérsic model. The vertical axis represents flux in Jy. The dispersion of the observational data is indicated by the blue-filled area, with the blue line representing the median. Each model component is shown as a line with its corresponding color. The disk components are omitted for NGC 1097 to highlight their minor contribution to the model (see text for details).

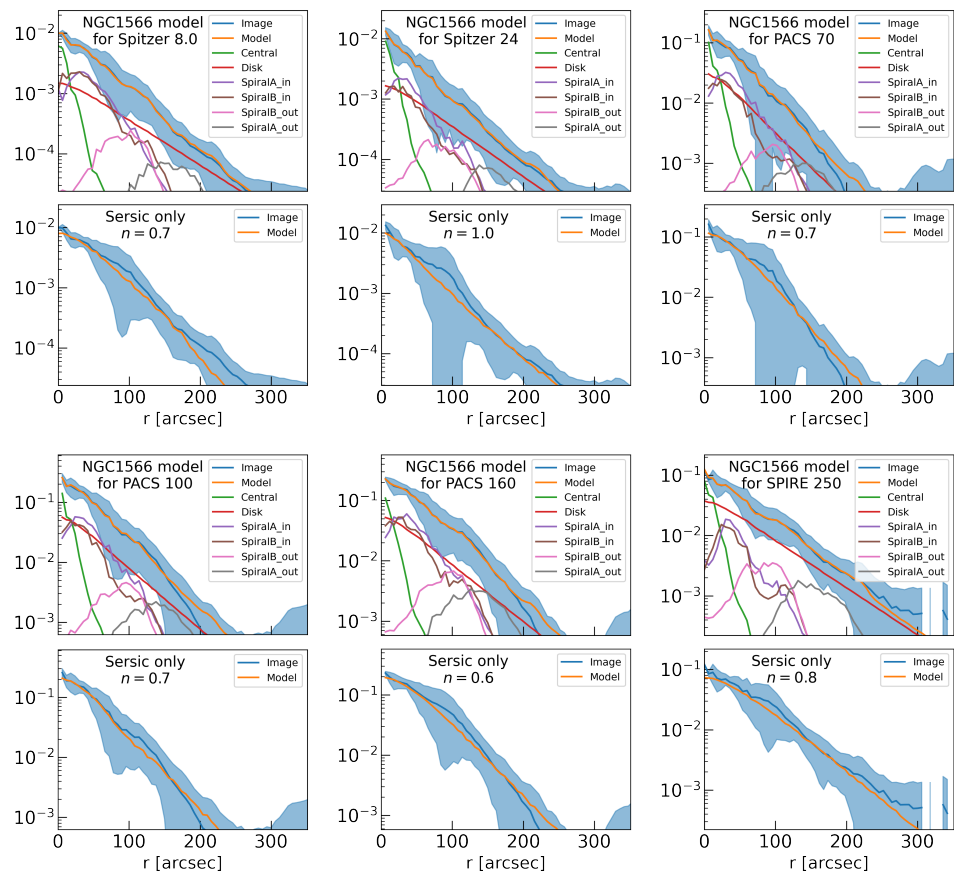


Figure A2. Same as Figure A1, but for NGC 1566.

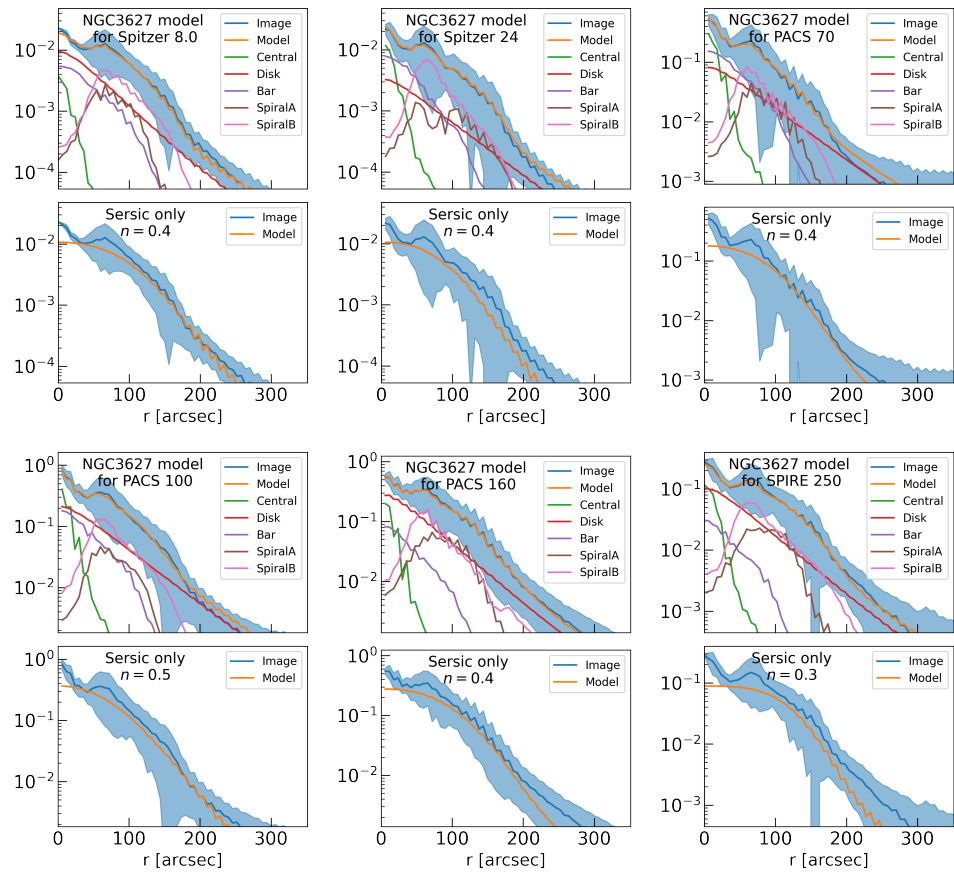


Figure A3. Same as Figure A1, but for NGC 3627.

Appendix B. HerBIE SED Fitting Example

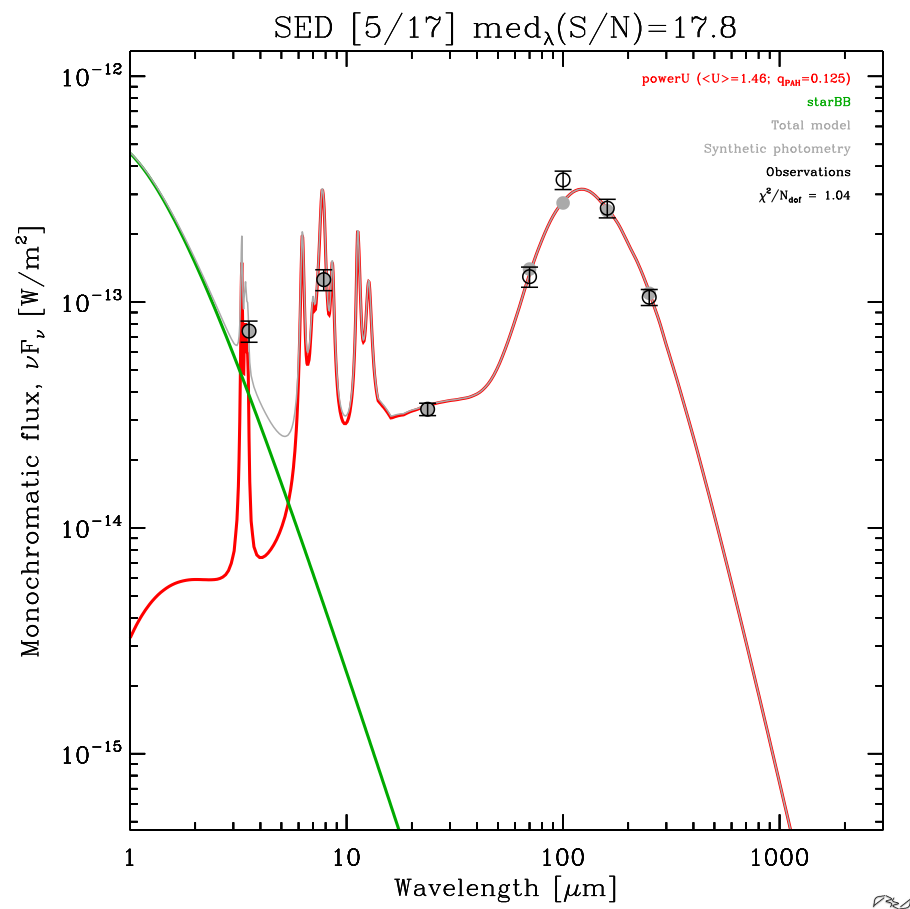


Figure A4. Example of SED fitting using HerBIE for Spiral B in NGC 1097.

Notes

- ¹ <http://dustpedia.astro.noa.gr/> (accessed on 10 June 2024).
- ² <https://archive.eso.org/dss/dss> (accessed on 10 June 2024).
- ³ <https://irsa.ipac.caltech.edu/> (accessed on 10 June 2024).
- ⁴ The latest version is available at https://github.com/IVChugunov/IMFIT_spirals (accessed on 20 March 2025).
- ⁵ Available at <http://www.ias.u-psud.fr/themis/> (accessed on 10 June 2024).

References

1. Popescu, C.C.; Tuffs, R.J. The percentage of stellar light re-radiated by dust in late-type Virgo Cluster galaxies. *Not. R. Astron. Soc.* **2002**, *335*, L41–L44. [\[CrossRef\]](#)
2. Wolfire, M.G.; Hollenbach, D.; McKee, C.F.; Tielens, A.G.G.M.; Bakes, E.L.O. The Neutral Atomic Phases of the Interstellar Medium. *Astrophys. J.* **1995**, *443*, 152. [\[CrossRef\]](#)
3. Draine, B.T. Photoelectric heating of interstellar gas. *Astrophys. J. Suppl.* **1978**, *36*, 595–619. [\[CrossRef\]](#)
4. Calzetti, D.; Kennicutt, R.C.; Engelbracht, C.W.; Leitherer, C.; Draine, B.T.; Kewley, L.; Moustakas, J.; Sosey, M.; Dale, D.A.; Gordon, K.D.; et al. The Calibration of Mid-Infrared Star Formation Rate Indicators. *Astrophys. J.* **2007**, *666*, 870–895. [\[CrossRef\]](#)
5. Kennicutt, R.C., Jr.; Hao, C.N.; Calzetti, D.; Moustakas, J.; Dale, D.A.; Bendo, G.; Engelbracht, C.W.; Johnson, B.D.; Lee, J.C. Dust-corrected Star Formation Rates of Galaxies. I. Combinations of H α and Infrared Tracers. *Astrophys. J.* **2009**, *703*, 1672–1695. [\[CrossRef\]](#)
6. Dopcke, G.; Glover, S.C.O.; Clark, P.C.; Klessen, R.S. The Effect of Dust Cooling on Low-metallicity Star-forming Clouds. *Astrophys. J.* **2011**, *729*, L3. [\[CrossRef\]](#)
7. Baes, M.; Dejonghe, H. Diffuse Dust and its Effects on the Kinematic Structure of Early-type Galaxies. In *Proceedings of the Dynamics of Galaxies: From the Early Universe to the Present*, Paris, France, 9–13 July 1999; Combes, F., Mamon, G.A., Charmandaris, V., Eds.; Astronomical Society of the Pacific Conference Series; NASA: Washington, DC, USA, 2000; Volume 197, p. 237.

8. Grosbøl, P.J.; Block, D.L.; Patsis, P.A. Dust Lanes in Spiral Galaxies. *Astrophys. Space Sci.* **1999**, *269*–270, 423–426. [\[CrossRef\]](#)
9. Köhler, M.; Ysard, N.; Jones, A.P. Dust evolution in the transition towards the denser ISM: Impact on dust temperature, opacity, and spectral index. *Astron. Astrophys.* **2015**, *579*, A15. [\[CrossRef\]](#)
10. Fisher, R.; Bowler, R.A.A.; Stefanon, M.; Rowland, L.E.; Algera, H.S.B.; Aravena, M.; Bouwens, R.; Dayal, P.; Ferrara, A.; Fudamoto, Y.; et al. REBELS-IFU: Dust attenuation curves of 12 massive galaxies at $z \simeq 7$. *arXiv* **2025**, arXiv:2501.10541. [\[CrossRef\]](#)
11. Algera, H.; Rowland, L.; Stefanon, M.; Palla, M.; Sommovigo, L.; Inami, H.; Bouwens, R.; Aravena, M.; Bowler, R.; Dayal, P.; et al. REBELS-IFU: Dust Build-up in Massive Galaxies at Redshift 7. *arXiv* **2025**, arXiv:2501.10508. [\[CrossRef\]](#)
12. Draine, B.T. Interstellar Dust Grains. *Annu. Rev. Astron. Astrophys.* **2003**, *41*, 241–289. [\[CrossRef\]](#)
13. Galliano, F.; Galametz, M.; Jones, A.P. The Interstellar Dust Properties of Nearby Galaxies. *Annu. Rev. Astron. Astrophys.* **2018**, *56*, 673–713. [\[CrossRef\]](#)
14. Popescu, C.C.; Misiriotis, A.; Kylafis, N.D.; Tuffs, R.J.; Fischera, J. Modelling the spectral energy distribution of galaxies. I. Radiation fields and grain heating in the edge-on spiral NGC 891. *Astron. Astrophys.* **2000**, *362*, 138–150. [\[CrossRef\]](#)
15. Alton, P.B.; Xilouris, E.M.; Misiriotis, A.; Dasyra, K.M.; Dumke, M. The emissivity of dust grains in spiral galaxies. *Astron. Astrophys.* **2004**, *425*, 109–120. [\[CrossRef\]](#)
16. Baes, M.; Fritz, J.; Gadotti, D.A.; Smith, D.J.B.; Dunne, L.; da Cunha, E.; Amblard, A.; Auld, R.; Bendo, G.J.; Bonfield, D.; et al. Herschel-ATLAS: The dust energy balance in the edge-on spiral galaxy UGC 4754. *Astron. Astrophys.* **2010**, *518*, L39. [\[CrossRef\]](#)
17. De Looze, I.; Baes, M.; Bendo, G.J.; Ciesla, L.; Cortese, L.; de Geyter, G.; Groves, B.; Boquien, M.; Boselli, A.; Brondeel, L.; et al. The dust energy balance in the edge-on spiral galaxy NGC 4565. *Not. R. Astron. Soc.* **2012**, *427*, 2797–2811. [\[CrossRef\]](#)
18. Mosenkov, A.V.; Allaert, F.; Baes, M.; Bianchi, S.; Camps, P.; De Geyter, G.; De Looze, I.; Fritz, J.; Gentile, G.; Hughes, T.M.; et al. HERschel Observations of Edge-on Spirals (HEROES). III. Dust energy balance study of IC 2531. *Astron. Astrophys.* **2016**, *592*, A71. [\[CrossRef\]](#)
19. Mosenkov, A.V.; Allaert, F.; Baes, M.; Bianchi, S.; Camps, P.; Clark, C.J.R.; Declair, M.; De Geyter, G.; De Looze, I.; Fritz, J.; et al. HERschel Observations of Edge-on Spirals (HEROES). IV. Dust energy balance problem. *Astron. Astrophys.* **2018**, *616*, A120. [\[CrossRef\]](#)
20. Bendo, G.J.; Boselli, A.; Dariush, A.; Pohlen, M.; Roussel, H.; Sauvage, M.; Smith, M.W.L.; Wilson, C.D.; Baes, M.; Cooray, A.; et al. Investigations of dust heating in M81, M83 and NGC 2403 with the Herschel Space Observatory. *Not. R. Astron. Soc.* **2012**, *419*, 1833–1859. [\[CrossRef\]](#)
21. Nersesian, A.; Xilouris, E.M.; Bianchi, S.; Galliano, F.; Jones, A.P.; Baes, M.; Casasola, V.; Cassarà, L.P.; Clark, C.J.R.; Davies, J.I.; et al. Old and young stellar populations in DustPedia galaxies and their role in dust heating. *Astron. Astrophys.* **2019**, *624*, A80. [\[CrossRef\]](#)
22. Nersesian, A.; Verstocken, S.; Viaene, S.; Baes, M.; Xilouris, E.M.; Bianchi, S.; Casasola, V.; Clark, C.J.R.; Davies, J.I.; De Looze, I.; et al. High-resolution, 3D radiative transfer modelling. III. The DustPedia barred galaxies. *Astron. Astrophys.* **2020**, *637*, A25. [\[CrossRef\]](#)
23. Misiriotis, A.; Kylafis, N.D.; Papamastorakis, J.; Xilouris, E.M. Is the exponential distribution a good approximation of dusty galactic disks? *Astron. Astrophys.* **2000**, *353*, 117–123. [\[CrossRef\]](#)
24. Muñoz-Mateos, J.C.; Gil de Paz, A.; Boissier, S.; Zamorano, J.; Dale, D.A.; Pérez-González, P.G.; Gallego, J.; Madore, B.F.; Bendo, G.; Thornley, M.D.; et al. Radial Distribution of Stars, Gas, and Dust in SINGS Galaxies. II. Derived Dust Properties. *Astrophys. J.* **2009**, *701*, 1965–1991. [\[CrossRef\]](#)
25. Mosenkov, A.V.; Baes, M.; Bianchi, S.; Casasola, V.; Cassarà, L.P.; Clark, C.J.R.; Davies, J.; De Looze, I.; De Vis, P.; Fritz, J.; et al. Dust emission profiles of DustPedia galaxies. *Astron. Astrophys.* **2019**, *622*, A132. [\[CrossRef\]](#)
26. Mattsson, L.; Andersen, A.C. On the dust abundance gradients in late-type galaxies—II. Analytical models as evidence for massive interstellar dust growth in SINGS galaxies. *Not. R. Astron. Soc.* **2012**, *423*, 38–48. [\[CrossRef\]](#)
27. Viaene, S.; Baes, M.; Tamm, A.; Tempel, E.; Bendo, G.; Blommaert, J.A.D.L.; Boquien, M.; Boselli, A.; Camps, P.; Cooray, A.; et al. The Herschel Exploitation of Local Galaxy Andromeda (HELGA). VII. A SKIRT radiative transfer model and insights on dust heating. *Astron. Astrophys.* **2017**, *599*, A64. [\[CrossRef\]](#)
28. Williams, T.G.; Baes, M.; De Looze, I.; Relaño, M.; Smith, M.W.L.; Verstocken, S.; Viaene, S. High-resolution radiative transfer modelling of M33. *Not. R. Astron. Soc.* **2019**, *487*, 2753–2770. [\[CrossRef\]](#)
29. Verstocken, S.; Nersesian, A.; Baes, M.; Viaene, S.; Bianchi, S.; Casasola, V.; Clark, C.J.R.; Davies, J.I.; De Looze, I.; De Vis, P.; et al. High-resolution, 3D radiative transfer modelling. II. The early-type spiral galaxy M 81. *Astron. Astrophys.* **2020**, *637*, A24. [\[CrossRef\]](#)
30. Nersesian, A.; Viaene, S.; De Looze, I.; Baes, M.; Xilouris, E.M.; Smith, M.W.L.; Bianchi, S.; Casasola, V.; Cassarà, L.P.; Clark, C.J.R.; et al. High-resolution, 3D radiative transfer modelling. V. A detailed model of the M 51 interacting pair. *Astron. Astrophys.* **2020**, *643*, A90. [\[CrossRef\]](#)
31. Thirlwall, J.J.; Popescu, C.C.; Tuffs, R.J.; Natale, G.; Norris, M.; Rushton, M.; Grootes, M.; Carroll, B. A radiative transfer model for the spiral galaxy M33. *Not. R. Astron. Soc.* **2020**, *495*, 835–863. [\[CrossRef\]](#)

32. Inman, C.J.; Popescu, C.C.; Rushton, M.T.; Murphy, D. Deriving the intrinsic properties of M51 with radiative transfer models. *Not. R. Astron. Soc.* **2023**, *526*, 118–137. [[CrossRef](#)]
33. Xilouris, E.M.; Kylafis, N.D.; Papamastorakis, J.; Paleologou, E.V.; Haerendel, G. The distribution of stars and dust in spiral galaxies: The edge-on spiral UGC 2048. *Astron. Astrophys.* **1997**, *325*, 135–143.
34. Bianchi, S. The dust distribution in edge-on galaxies. Radiative transfer fits of V and K'-band images. *Astron. Astrophys.* **2007**, *471*, 765–773. [[CrossRef](#)]
35. De Geyter, G.; Baes, M.; Fritz, J.; Camps, P. FitSKIRT: Genetic algorithms to automatically fit dusty galaxies with a Monte Carlo radiative transfer code. *Astron. Astrophys.* **2013**, *550*, A74. [[CrossRef](#)]
36. Baes, M.; Verstackpen, J.; De Looze, I.; Fritz, J.; Saftly, W.; Vidal Pérez, E.; Stalevski, M.; Valcke, S. Efficient Three-dimensional NLTE Dust Radiative Transfer with SKIRT. *Astrophys. J. Suppl.* **2011**, *196*, 22. [[CrossRef](#)]
37. Camps, P.; Baes, M. SKIRT: An advanced dust radiative transfer code with a user-friendly architecture. *Astron. Comput.* **2015**, *9*, 20–33. [[CrossRef](#)]
38. Galliano, F.; Nersesian, A.; Bianchi, S.; De Looze, I.; Roychowdhury, S.; Baes, M.; Casasola, V.; Cassará, L.P.; Dobbels, W.; Fritz, J.; et al. A nearby galaxy perspective on dust evolution. Scaling relations and constraints on the dust build-up in galaxies with the DustPedia and DGS samples. *Astron. Astrophys.* **2021**, *649*, A18. [[CrossRef](#)]
39. Dale, D.A.; Boquien, M.; Turner, J.A.; Calzetti, D.; Kennicutt, R.C.; Lee, J.C. Spectral Energy Distributions for 258 Local Volume Galaxies. *Astron. J.* **2023**, *165*, 260. [[CrossRef](#)]
40. Boselli, A.; Ciesla, L.; Buat, V.; Cortese, L.; Auld, R.; Baes, M.; Bendo, G.J.; Bianchi, S.; Bock, J.; Bomans, D.J.; et al. FIR colours and SEDs of nearby galaxies observed with Herschel. *Astron. Astrophys.* **2010**, *518*, L61. [[CrossRef](#)]
41. Aniano, G.; Draine, B.T.; Calzetti, D.; Dale, D.A.; Engelbracht, C.W.; Gordon, K.D.; Hunt, L.K.; Kennicutt, R.C.; Krause, O.; Leroy, A.K.; et al. Modeling Dust and Starlight in Galaxies Observed by Spitzer and Herschel: NGC 628 and NGC 6946. *Astrophys. J.* **2012**, *756*, 138. [[CrossRef](#)]
42. Chasteney, J.; Sandstrom, K.; Leroy, A.K.; Bot, C.; Chiang, I.D.; Chown, R.; Gordon, K.D.; Koch, E.W.; Roussel, H.; Sutter, J.; et al. The Resolved Behavior of Dust Mass, Polycyclic Aromatic Hydrocarbon Fraction, and Radiation Field in ~800 Nearby Galaxies. *Astrophys. J. Suppl.* **2025**, *276*, 2. [[CrossRef](#)]
43. Abdurro'uf, Y.T.; Hirashita, H.; Morishita, T.; Tacchella, S.; Akiyama, M.; Takeuchi, T.T.; Wu, P.F. Dissecting Nearby Galaxies with piXedfit. I. Spatially Resolved Properties of Stars, Dust, and Gas as Revealed by Panchromatic SED Fitting. *Astrophys. J.* **2022**, *926*, 81. [[CrossRef](#)]
44. Scaloni, L.; Rodighiero, G.; Enia, A.; Gruppioni, C.; Annibali, F.; Bisigello, L.; Cassata, P.; Corsini, E.M.; Casasola, V.; Lofaro, C.M.; et al. The impact of stellar bars on star-formation quenching: Insights from a spatially resolved analysis in the local Universe. *Astron. Astrophys.* **2024**, *687*, A255. [[CrossRef](#)]
45. Sun, B.; Calzetti, D.; Battisti, A.J. The Role of Spiral Arms in Galaxies. *Astrophys. J.* **2024**, *973*, 137. [[CrossRef](#)]
46. Boquien, M.; Burgarella, D.; Roehlly, Y.; Buat, V.; Ciesla, L.; Corre, D.; Inoue, A.K.; Salas, H. CIGALE: A python Code Investigating GALaxy Emission. *Astron. Astrophys.* **2019**, *622*, A103. [[CrossRef](#)]
47. da Cunha, E.; Charlot, S.; Elbaz, D. A simple model to interpret the ultraviolet, optical and infrared emission from galaxies. *Not. R. Astron. Soc.* **2008**, *388*, 1595–1617. [[CrossRef](#)]
48. Kriek, M.; van Dokkum, P.G.; Labbé, I.; Franx, M.; Illingworth, G.D.; Marchesini, D.; Quadri, R.F. An Ultra-Deep Near-Infrared Spectrum of a Compact Quiescent Galaxy at $z = 2.2$. *Astrophys. J.* **2009**, *700*, 221–231. [[CrossRef](#)]
49. Galliano, F. A dust spectral energy distribution model with hierarchical Bayesian inference—I. Formalism and benchmarking. *Not. R. Astron. Soc.* **2018**, *476*, 1445–1469. [[CrossRef](#)]
50. Jones, A.P.; Köhler, M.; Ysard, N.; Bocchio, M.; Verstraete, L. The global dust modelling framework THEMIS. *Astron. Astrophys.* **2017**, *602*, A46. [[CrossRef](#)]
51. Hensley, B.S.; Draine, B.T. The Astrodust+PAH Model: A Unified Description of the Extinction, Emission, and Polarization from Dust in the Diffuse Interstellar Medium. *Astrophys. J.* **2023**, *948*, 55. [[CrossRef](#)]
52. da Cunha, E.; Eminian, C.; Charlot, S.; Blaizot, J. New insight into the relation between star formation activity and dust content in galaxies. *Not. R. Astron. Soc.* **2010**, *403*, 1894–1908. [[CrossRef](#)]
53. Cortese, L.; Ciesla, L.; Boselli, A.; Bianchi, S.; Gomez, H.; Smith, M.W.L.; Bendo, G.J.; Eales, S.; Pohlen, M.; Baes, M.; et al. The dust scaling relations of the Herschel Reference Survey. *Astron. Astrophys.* **2012**, *540*, A52. [[CrossRef](#)]
54. Erwin, P. IMFIT: A Fast, Flexible New Program for Astronomical Image Fitting. *Astrophys. J.* **2015**, *799*, 226. [[CrossRef](#)]
55. Peng, C.Y.; Ho, L.C.; Impey, C.D.; Rix, H.W. Detailed Decomposition of Galaxy Images. II. Beyond Axisymmetric Models. *Astron. J.* **2010**, *139*, 2097–2129. [[CrossRef](#)]
56. Savchenko, S.S.; Poliakov, D.M.; Mosenkov, A.V.; Smirnov, A.A.; Marchuk, A.A.; Il'in, V.B.; Gontcharov, G.A.; Seguíne, J.; Baes, M. The problem of dust attenuation in photometric decomposition of edge-on galaxies and possible solutions. *Not. R. Astron. Soc.* **2023**, *524*, 4729–4745. [[CrossRef](#)]

57. Gong, J.Y.; Mao, Y.W.; Gao, H.; Yu, S.Y. Multiwavelength Bulge-Disk Decomposition for the Galaxy M81 (NGC 3031). I. Morphology. *Astrophys. J. Suppl.* **2023**, *267*, 26. [\[CrossRef\]](#)
58. Conselice, C.J. The fundamental properties of galaxies and a new galaxy classification system. *Not. R. Astron. Soc.* **2006**, *373*, 1389–1408. [\[CrossRef\]](#)
59. Willett, K.W.; Lintott, C.J.; Bamford, S.P.; Masters, K.L.; Simmons, B.D.; Casteels, K.R.V.; Edmondson, E.M.; Fortson, L.F.; Kaviraj, S.; Keel, W.C.; et al. Galaxy Zoo 2: Detailed morphological classifications for 304 122 galaxies from the Sloan Digital Sky Survey. *Not. R. Astron. Soc.* **2013**, *435*, 2835–2860. [\[CrossRef\]](#)
60. Chugunov, I.V.; Marchuk, A.A.; Mosenkov, A.V. Less Wound and More Asymmetric: JWST Confirms the Evolution of Spiral Structure in Galaxies at $z \lesssim 3$. *arXiv* **2025**, arXiv:2501.11670. [\[CrossRef\]](#)
61. Kuhn, V.; Guo, Y.; Martin, A.; Bayless, J.; Gates, E.; Puleo, A. JWST Reveals a Surprisingly High Fraction of Galaxies Being Spiral-like at $0.5 \leq z \leq 4$. *Astrophys. J.* **2024**, *968*, L15. [\[CrossRef\]](#)
62. Salcedo, J.M.E.; Pastras, S.; Vácha, J.; Pulsoni, C.; Genzel, R.; Schreiber, N.M.F.; Jolly, J.B.; Barfety, C.; Chen, J.; Tozzi, G.; et al. Galaxy Morphologies at Cosmic Noon with JWST: A Foundation for Exploring Gas Transport with Bars and Spiral Arms. *arXiv* **2025**, arXiv:2503.21738v1.
63. Savchenko, S.; Marchuk, A.; Mosenkov, A.; Grishunin, K. A multiwavelength study of spiral structure in galaxies. I. General characteristics in the optical. *Not. R. Astron. Soc.* **2020**, *493*, 390–409. [\[CrossRef\]](#)
64. Marchuk, A.A.; Chugunov, I.V.; Gontcharov, G.A.; Mosenkov, A.V.; Il'in, V.B.; Savchenko, S.S.; Smirnov, A.A.; Poliakov, D.M.; Seguin, J.; Chazov, M.I. Galaxies decomposition with spiral arms—II. A multiwavelength case study of M 51. *Not. R. Astron. Soc.* **2024**, *528*, 1276–1295. [\[CrossRef\]](#)
65. Chugunov, I.V.; Marchuk, A.A.; Mosenkov, A.V.; Savchenko, S.S.; Shishkina, E.V.; Chazov, M.I.; Nazarova, A.E.; Skryabina, M.N.; Smirnova, P.I.; Smirnov, A.A. Galaxies decomposition with spiral arms—I: 29 galaxies from S⁴G. *Not. R. Astron. Soc.* **2024**, *527*, 9605–9624. [\[CrossRef\]](#)
66. White, R.E., III; Keel, W.C.; Conselice, C.J. Seeing Galaxies through Thick and Thin. I. Optical Opacity Measures in Overlapping Galaxies. *Astrophys. J.* **2000**, *542*, 761–778. [\[CrossRef\]](#)
67. Khoperskov, S.; Di Matteo, P.; Haywood, M.; Combes, F. Stellar metallicity variations across spiral arms in disk galaxies with multiple populations. *Astron. Astrophys.* **2018**, *611*, L2. [\[CrossRef\]](#)
68. Popescu, C.C.; Tuffs, R.J. Modelling the SEDs of spiral galaxies. *Eur. Astron. Soc. Publ. Ser.* **2009**, *34*, 247–256. [\[CrossRef\]](#)
69. Schechtman-Rook, A.; Bershadsky, M.A.; Wood, K. The Three-dimensional Distribution of Dust in NGC 891. *Astrophys. J.* **2012**, *746*, 70. [\[CrossRef\]](#)
70. Gebek, A.; Diemer, B.; Martorano, M.; van der Wel, A.; Pantoni, L.; Baes, M.; Gabrielpillai, A.; Kapoor, A.U.; Osinga, C.; Nersesian, A.; et al. The mass-dependent UVJ diagram at cosmic noon: A challenge for galaxy evolution models and dust radiative transfer. *arXiv* **2025**, arXiv:2501.12008. [\[CrossRef\]](#)
71. Rushton, M.T.; Popescu, C.C.; Inman, C.; Natale, G.; Pricopi, D. Decoding NGC 628 with radiative transfer methods. *Not. R. Astron. Soc.* **2022**, *514*, 113–138. [\[CrossRef\]](#)
72. Pricopi, D.; Popescu, C.C.; Rushton, M.T.; Murphy, D.; Inman, C.J.; Toma, R. Uncovering the truth about M101, NGC 3938, and their significant others through radiative transfer. *Not. R. Astron. Soc.* **2025**, *537*, 56–83. [\[CrossRef\]](#)
73. Querejeta, M.; Leroy, A.K.; Meidt, S.E.; Schinnerer, E.; Belfiore, F.; Emsellem, E.; Klessen, R.S.; Sun, J.; Sormani, M.; Bešlić, I.; et al. Do spiral arms enhance star formation efficiency? *Astron. Astrophys.* **2024**, *687*, A293. [\[CrossRef\]](#)
74. Vogler, A.; Madden, S.C.; Beck, R.; Lundgren, A.A.; Sauvage, M.; Vigroux, L.; Ehle, M. Dissecting the spiral galaxy M 83: Mid-infrared emission and comparison with other tracers of star formation. *Astron. Astrophys.* **2005**, *441*, 491–511. [\[CrossRef\]](#)
75. Gao, H.; Ho, L.C. An Optimal Strategy for Accurate Bulge-to-disk Decomposition of Disk Galaxies. *Astrophys. J.* **2017**, *845*, 114. [\[CrossRef\]](#)
76. Salo, H.; Laurikainen, E.; Laine, J.; Comerón, S.; Gadotti, D.A.; Buta, R.; Sheth, K.; Zaritsky, D.; Ho, L.; Knapen, J.; et al. The Spitzer Survey of Stellar Structure in Galaxies (S⁴G): Multi-component Decomposition Strategies and Data Release. *Astrophys. J. Suppl.* **2015**, *219*, 4. [\[CrossRef\]](#)
77. Clark, C.J.R.; Verstocken, S.; Bianchi, S.; Fritz, J.; Viaene, S.; Smith, M.W.L.; Baes, M.; Casasola, V.; Cassara, L.P.; Davies, J.I.; et al. DustPedia: Multiwavelength photometry and imagery of 875 nearby galaxies in 42 ultraviolet-microwave bands. *Astron. Astrophys.* **2018**, *609*, A37. [\[CrossRef\]](#)
78. Miller, R.; Kenefick, D.; Kenefick, J.; Shameer Abdeen, M.; Monson, E.; Eufrazio, R.T.; Shields, D.W.; Davis, B.L. Investigating the Origins of Spiral Structure in Disk Galaxies through a Multiwavelength Study. *Astrophys. J.* **2019**, *874*, 177. [\[CrossRef\]](#)
79. Koekemoer, A.M.; Aussel, H.; Calzetti, D.; Capak, P.; Giavalisco, M.; Kneib, J.P.; Leauthaud, A.; Le Fèvre, O.; McCracken, H.J.; Massey, R.; et al. The COSMOS Survey: Hubble Space Telescope Advanced Camera for Surveys Observations and Data Processing. *Astrophys. J. Suppl.* **2007**, *172*, 196–202. [\[CrossRef\]](#)

80. Bagley, M.B.; Finkelstein, S.L.; Koekemoer, A.M.; Ferguson, H.C.; Arrabal Haro, P.; Dickinson, M.; Kartaltepe, J.S.; Papovich, C.; Pérez-González, P.G.; Pirzkal, N.; et al. CEERS Epoch 1 NIRC2 Imaging: Reduction Methods and Simulations Enabling Early JWST Science Results. *Astrophys. J.* **2023**, *946*, L12. [\[CrossRef\]](#)
81. Bunker, A.J.; Cameron, A.J.; Curtis-Lake, E.; Jakobsen, P.; Carniani, S.; Curti, M.; Witstok, J.; Maiolino, R.; D'Eugenio, F.; Looser, T.J.; et al. JADES NIRSpec initial data release for the Hubble Ultra Deep Field: Redshifts and line fluxes of distant galaxies from the deepest JWST Cycle 1 NIRSpec multi-object spectroscopy. *Astron. Astrophys.* **2024**, *690*, A288. [\[CrossRef\]](#)
82. Reshetnikov, V.P.; Marchuk, A.A.; Chugunov, I.V.; Usachev, P.A.; Mosenkov, A.V. Evolution of the Spiral Structure of Galaxies from HST COSMOS Field Data. *Astron. Lett.* **2022**, *48*, 644–652. [\[CrossRef\]](#)
83. Reshetnikov, V.P.; Marchuk, A.A.; Chugunov, I.V.; Usachev, P.A.; Mosenkov, A.V. The possible evolution of pitch angles of spiral galaxies. *Astron. Astrophys.* **2023**, *680*, L14. [\[CrossRef\]](#)
84. Funakoshi, N.; Matsunaga, N.; Kawata, D.; Baba, J.; Taniguchi, D.; Fujii, M. Clues to growth and disruption of two neighbouring spiral arms of the Milky Way. *Not. R. Astron. Soc.* **2024**, *533*, 4324–4333. [\[CrossRef\]](#)
85. Lin, C.C.; Shu, F.H. On the Spiral Structure of Disk Galaxies. *Astrophys. J.* **1964**, *140*, 646. [\[CrossRef\]](#)
86. Lin, C.C.; Shu, F.H. Density waves in disk galaxies. In *Proceedings of the Radio Astronomy and the Galactic System*, Noordwijk, The Netherlands, 25 August–1 September 1967; van Woerden, H., Ed.; Academic Press: London, UK, 1967; Volume 31, p. 313.
87. Roberts, W.W. Large-Scale Shock Formation in Spiral Galaxies and its Implications on Star Formation. *Astrophys. J.* **1969**, *158*, 123. [\[CrossRef\]](#)
88. Bertin, G.; Lin, C.C.; Lowe, S.A.; Thurstans, R.P. Modal Approach to the Morphology of Spiral Galaxies. II. Dynamical Mechanisms. *Astrophys. J.* **1989**, *338*, 104. [\[CrossRef\]](#)
89. Athanassoula, E. Manifold-driven spirals in N-body barred galaxy simulations. *Not. R. Astron. Soc.* **2012**, *426*, L46–L50. [\[CrossRef\]](#)
90. Romero-Gómez, M.; Athanassoula, E.; Masdemont, J.J.; García-Gómez, C. The formation of spiral arms and rings in barred galaxies. *Astron. Astrophys.* **2007**, *472*, 63–75. [\[CrossRef\]](#)
91. Toomre, A. Group Velocity of Spiral Waves in Galactic Disks. *Astrophys. J.* **1969**, *158*, 899. [\[CrossRef\]](#)
92. Julian, W.H.; Toomre, A. Non-Axisymmetric Responses of Differentially Rotating Disks of Stars. *Astrophys. J.* **1966**, *146*, 810. [\[CrossRef\]](#)
93. Sellwood, J.A.; Carlberg, R.G. Spiral instabilities provoked by accretion and star formation. *Astrophys. J.* **1984**, *282*, 61–74. [\[CrossRef\]](#)
94. Sellwood, J.A. The lifetimes of spiral patterns in disc galaxies. *Not. R. Astron. Soc.* **2011**, *410*, 1637–1646. [\[CrossRef\]](#)
95. Sellwood, J.A.; Carlberg, R.G. Spiral instabilities: Mechanism for recurrence. *Not. R. Astron. Soc.* **2019**, *489*, 116–131. [\[CrossRef\]](#)
96. Dobbs, C.L.; Pringle, J.E. Age distributions of star clusters in spiral and barred galaxies as a test for theories of spiral structure. *Not. R. Astron. Soc.* **2010**, *409*, 396–404. [\[CrossRef\]](#)
97. Sellwood, J.A.; Masters, K.L. Spirals in galaxies. *arXiv* **2021**, arXiv:2110.05615.
98. Dobbs, C.; Baba, J. Dawes Review 4: Spiral Structures in Disc Galaxies. *Publ. Astron. Soc. Aust.* **2014**, *31*, e035. [\[CrossRef\]](#)
99. Shu, F.H. Six Decades of Spiral Density Wave Theory. *Annu. Rev. Astron. Astrophys.* **2016**, *54*, 667–724. [\[CrossRef\]](#)
100. Tamburro, D.; Rix, H.W.; Walter, F.; Brinks, E.; de Blok, W.J.G.; Kennicutt, R.C.; Mac Low, M.M. Geometrically Derived Timescales for Star Formation in Spiral Galaxies. *Astron. J.* **2008**, *136*, 2872–2885. [\[CrossRef\]](#)
101. Chang, Y.Y.; van der Wel, A.; da Cunha, E.; Rix, H.W. Stellar Masses and Star Formation Rates for 1M Galaxies from SDSS+WISE. *Astrophys. J. Suppl.* **2015**, *219*, 8. [\[CrossRef\]](#)
102. Devereux, N.A.; Young, J.S. The Origin of the Far-Infrared Luminosity from Spiral Galaxies. *Astrophys. J.* **1990**, *350*, L25. [\[CrossRef\]](#)
103. Galametz, M.; Kennicutt, R.C.; Albrecht, M.; Aniano, G.; Armus, L.; Bertoldi, F.; Calzetti, D.; Crocker, A.F.; Croxall, K.V.; Dale, D.A.; et al. Mapping the cold dust temperatures and masses of nearby KINGFISH galaxies with Herschel. *Not. R. Astron. Soc.* **2012**, *425*, 763–787. [\[CrossRef\]](#)
104. Auld, R.; Bianchi, S.; Smith, M.W.L.; Davies, J.I.; Bendo, G.J.; di Serego, S.A.; Cortese, L.; Baes, M.; Bomans, D.J.; Boquien, M.; et al. The Herschel Virgo Cluster Survey—XII. FIR properties of optically selected Virgo cluster galaxies. *Not. R. Astron. Soc.* **2013**, *428*, 1880–1910. [\[CrossRef\]](#)
105. Cortese, L.; Fritz, J.; Bianchi, S.; Boselli, A.; Ciesla, L.; Bendo, G.J.; Boquien, M.; Roussel, H.; Baes, M.; Buat, V.; et al. PACS photometry of the Herschel Reference Survey—Far-infrared/submillimetre colours as tracers of dust properties in nearby galaxies. *Not. R. Astron. Soc.* **2014**, *440*, 942–956. [\[CrossRef\]](#)
106. Davies, J.I.; Baes, M.; Bianchi, S.; Jones, A.; Madden, S.; Xilouris, M.; Bocchio, M.; Casasola, V.; Cassara, L.; Clark, C.; et al. DustPedia: A Definitive Study of Cosmic Dust in the Local Universe. *Publ. Astron. Soc. Pac.* **2017**, *129*, 044102. [\[CrossRef\]](#)
107. Pilbratt, G.L.; Riedinger, J.R.; Passvogel, T.; Crone, G.; Doyle, D.; Gageur, U.; Heras, A.M.; Jewell, C.; Metcalfe, L.; Ott, S.; et al. Herschel Space Observatory. An ESA facility for far-infrared and submillimetre astronomy. *Astron. Astrophys.* **2010**, *518*, L1. [\[CrossRef\]](#)

108. Skrutskie, M.F.; Cutri, R.M.; Stiening, R.; Weinberg, M.D.; Schneider, S.; Carpenter, J.M.; Beichman, C.; Capps, R.; Chester, T.; Elias, J.; et al. The Two Micron All Sky Survey (2MASS). *Astron. J.* **2006**, *131*, 1163–1183. [\[CrossRef\]](#)
109. Wright, E.L.; Eisenhardt, P.R.M.; Mainzer, A.K.; Ressler, M.E.; Cutri, R.M.; Jarrett, T.; Kirkpatrick, J.D.; Padgett, D.; McMillan, R.S.; Skrutskie, M.; et al. The Wide-field Infrared Survey Explorer (WISE): Mission Description and Initial On-orbit Performance. *Astron. J.* **2010**, *140*, 1868–1881. [\[CrossRef\]](#)
110. Werner, M.W.; Roellig, T.L.; Low, F.J.; Rieke, G.H.; Rieke, M.; Hoffmann, W.F.; Young, E.; Houck, J.R.; Brandl, B.; Fazio, G.G.; et al. The Spitzer Space Telescope Mission. *Astrophys. J. Suppl.* **2004**, *154*, 1. [\[CrossRef\]](#)
111. Neugebauer, G.; Habing, H.J.; van Duinen, R.; Aumann, H.H.; Baud, B.; Beichman, C.A.; Beintema, D.A.; Boggess, N.; Clegg, P.E.; de Jong, T.; et al. The Infrared Astronomical Satellite (IRAS) mission. *Astrophys. J.* **1984**, *278*, L1–L6. [\[CrossRef\]](#)
112. Ade, P.A.R. et al. [Planck Collaboration]. Planck early results. I. The Planck mission. *Astron. Astrophys.* **2011**, *536*, A1. [\[CrossRef\]](#)
113. Morrissey, P.; Conrow, T.; Barlow, T.A.; Small, T.; Seibert, M.; Wyder, T.K.; Budavári, T.; Arnouts, S.; Friedman, P.G.; Forster, K.; et al. The Calibration and Data Products of GALEX. *Astrophys. J. Suppl.* **2007**, *173*, 682–697. [\[CrossRef\]](#)
114. York, D.G.; Adelmann, J.; Anderson, John E., Jr.; Anderson, S.F.; Annis, J.; Bahcall, N.A.; Bakken, J.A.; Barkhouser, R.; Bastian, S.; Berman, E.; et al. The Sloan Digital Sky Survey: Technical Summary. *Astron. J.* **2000**, *120*, 1579–1587. [\[CrossRef\]](#)
115. Griffin, M.J.; Abergel, A.; Abreu, A.; Ade, P.A.R.; André, P.; Augeres, J.L.; Babbedge, T.; Bae, Y.; Baillie, T.; Baluteau, J.P.; et al. The Herschel-SPIRE instrument and its in-flight performance. *Astron. Astrophys.* **2010**, *518*, L3. [\[CrossRef\]](#)
116. Poglitsch, A.; Waelkens, C.; Geis, N.; Feuchtgruber, H.; Vandenbussche, B.; Rodriguez, L.; Krause, O.; Renotte, E.; van Hoof, C.; Saraceno, P.; et al. The Photodetector Array Camera and Spectrometer (PACS) on the Herschel Space Observatory. *Astron. Astrophys.* **2010**, *518*, L2. [\[CrossRef\]](#)
117. Fazio, G.G.; Hora, J.L.; Allen, L.E.; Ashby, M.L.N.; Barmby, P.; Deutsch, L.K.; Huang, J.S.; Kleiner, S.; Marengo, M.; Megeath, S.T.; et al. The Infrared Array Camera (IRAC) for the Spitzer Space Telescope. *Astrophys. J. Suppl.* **2004**, *154*, 10–17. [\[CrossRef\]](#)
118. Aniano, G.; Draine, B.T.; Gordon, K.D.; Sandstrom, K. Common-Resolution Convolution Kernels for Space- and Ground-Based Telescopes. *Publ. Astron. Soc. Pac.* **2011**, *123*, 1218. [\[CrossRef\]](#)
119. Bradley, L.; Sipőcz, B.; Robitaille, T.; Tollerud, E.; Vinícius, Z.; Deil, C.; Barbary, K.; Wilson, T.J.; Busko, I.; Günther, H.M.; et al. *Astropy/Photutils: 1.0.0*; Zenodo: Genève, Switzerland, 2020. [\[CrossRef\]](#)
120. Román, J.; Trujillo, I.; Montes, M. Galactic cirri in deep optical imaging. *Astron. Astrophys.* **2020**, *644*, A42. [\[CrossRef\]](#)
121. Marchuk, A.A.; Smirnov, A.A.; Mosenkov, A.V.; Il'in, V.B.; Gontcharov, G.A.; Savchenko, S.S.; Román, J. Fractal dimension of optical cirrus in Stripe82. *Not. R. Astron. Soc.* **2021**, *508*, 5825–5841. [\[CrossRef\]](#)
122. Smirnov, A.A.; Savchenko, S.S.; Poliakov, D.M.; Marchuk, A.A.; Mosenkov, A.V.; Il'in, V.B.; Gontcharov, G.A.; Román, J.; Seguíne, J. Prospects for future studies using deep imaging: Analysis of individual Galactic cirrus filaments. *Not. R. Astron. Soc.* **2023**, *519*, 4735–4752. [\[CrossRef\]](#)
123. Anand, G.S.; Lee, J.C.; Van Dyk, S.D.; Leroy, A.K.; Rosolowsky, E.; Schinnerer, E.; Larson, K.; Kourkchi, E.; Kreckel, K.; Scheuermann, F.; et al. Distances to PHANGS galaxies: New tip of the red giant branch measurements and adopted distances. *Not. R. Astron. Soc.* **2021**, *501*, 3621–3639. [\[CrossRef\]](#)
124. Freedman, W.L.; Madore, B.F.; Gibson, B.K.; Ferrarese, L.; Kelson, D.D.; Sakai, S.; Mould, J.R.; Kennicutt, R.C., Jr.; Ford, H.C.; Graham, J.A.; et al. Final Results from the Hubble Space Telescope Key Project to Measure the Hubble Constant. *Astrophys. J.* **2001**, *553*, 47–72. [\[CrossRef\]](#)
125. Quillen, A.C.; Frogel, J.A.; Kuchinski, L.E.; Terndrup, D.M. Multiband Images of the Barred Galaxy NGC 1097. *Astron. J.* **1995**, *110*, 156. [\[CrossRef\]](#)
126. Kolcu, T.; Maciejewski, W.; Gadotti, D.A.; Fragkoudi, F.; Erwin, P.; Sánchez-Blázquez, P.; Neumann, J.; Van de Ven, G.; de Sá-Freitas, C.; Longmore, S.; et al. Composite bulges—IV. Detecting signatures of gas inflows in the IFU data: The MUSE view of ionized gas kinematics in NGC 1097. *Not. R. Astron. Soc.* **2023**, *524*, 207–223. [\[CrossRef\]](#)
127. Prieto, M.A.; Fernandez-Ontiveros, J.A.; Bruzual, G.; Burkert, A.; Schartmann, M.; Charlot, S. From kpcs to the central parsec of NGC 1097: Feeding star formation and a black hole at the same time. *Not. R. Astron. Soc.* **2019**, *485*, 3264–3276. [\[CrossRef\]](#)
128. Kotilainen, J.K.; Reunanen, J.; Laine, S.; Ryder, S.D. Near-infrared line imaging of the circumnuclear starburst rings in the active galaxies NGC 1097 and NGC 6574. *Astron. Astrophys.* **2000**, *353*, 834–846.
129. Barth, A.J.; Ho, L.C.; Filippenko, A.V.; Sargent, W.L. Hubble Space Telescope Observations of Circumnuclear Star-Forming Rings in NGC 1097 and NGC 6951. *Astron. J.* **1995**, *110*, 1009. [\[CrossRef\]](#)
130. Storchi-Bergmann, T.; Eracleous, M.; Livio, M.; Wilson, A.S.; Filippenko, A.V.; Halpern, J.P. The Variability of the Double-peaked Balmer Lines in the Active Nucleus of NGC 1097. *Astrophys. J.* **1995**, *443*, 617. [\[CrossRef\]](#)
131. Ho, L.C. Nuclear activity in nearby galaxies. *Annu. Rev. Astron. Astrophys.* **2008**, *46*, 475–539. [\[CrossRef\]](#)
132. Lewis, K.T.; Eracleous, M. Black Hole Masses of Active Galaxies with Double-peaked Balmer Emission Lines. *Astrophys. J.* **2006**, *642*, 711–719. [\[CrossRef\]](#)

133. Tomás, L.; Matzeu, G.A.; Jiménez Bailón, E.; Kalfountzou, E.; Santos-Lleó, M.; Parker, M.L.; Ballo, L.; Loiseau, N.; Ehle, M.; Rodríguez-Pascual, P.; et al. The changing-look AGN NGC 1566 in quiescence with XMM-Newton: A nuclear starburst and an AGN competing in power? *Not. R. Astron. Soc.* **2022**, *514*, 403–415. [\[CrossRef\]](#)
134. Oknyansky, V.L.; Winkler, H.; Tsygankov, S.S.; Lipunov, V.M.; Gorbovskoy, E.S.; van Wyk, F.; Buckley, D.A.H.; Tyurina, N.V. New changing look case in NGC 1566. *Not. R. Astron. Soc.* **2019**, *483*, 558–564. [\[CrossRef\]](#)
135. Liang, W.C.; Shu, X.W.; Wang, J.X.; Tan, Y.; Zhang, W.J.; Sun, L.M.; Jiang, N.; Dou, L.M. Response of the Fe K α line emission to the X-ray continuum variability in the changing-look active galactic nucleus NGC 1566. *J. High Energy Astrophys.* **2022**, *33*, 20–31. [\[CrossRef\]](#)
136. Parker, M.L.; Schartel, N.; Grupe, D.; Komossa, S.; Harrison, F.; Kollatschny, W.; Mikula, R.; Santos-Lleó, M.; Tomás, L. X-ray spectra reveal the reawakening of the repeat changing-look AGN NGC 1566. *Not. R. Astron. Soc.* **2019**, *483*, L88–L92. [\[CrossRef\]](#)
137. Woo, J.H.; Urry, C.M. Active Galactic Nucleus Black Hole Masses and Bolometric Luminosities. *Astrophys. J.* **2002**, *579*, 530–544. [\[CrossRef\]](#)
138. Jana, A.; Kumari, N.; Nandi, P.; Naik, S.; Chatterjee, A.; Jaisawal, G.K.; Hayasaki, K.; Ricci, C. Broad-band X-ray observations of the 2018 outburst of the changing-look active galactic nucleus NGC 1566. *Not. R. Astron. Soc.* **2021**, *507*, 687–703. [\[CrossRef\]](#)
139. Querejeta, M.; Schinnerer, E.; Meidt, S.; Sun, J.; Leroy, A.K.; Emsellem, E.; Klessen, R.S.; Muñoz-Mateos, J.C.; Salo, H.; Laurikainen, E.; et al. Stellar structures, molecular gas, and star formation across the PHANGS sample of nearby galaxies. *Astron. Astrophys.* **2021**, *656*, A133. [\[CrossRef\]](#)
140. Eibensteiner, C.; Sun, J.; Bigiel, F.; Leroy, A.K.; Schinnerer, E.; Rosolowsky, E.; Kurapati, S.; Pisano, D.J.; de Blok, W.J.G.; Barnes, A.T.; et al. PHANGS-MeerKAT and MHONGOOSE HI observations of nearby spiral galaxies: Physical drivers of the molecular gas fraction, R_{mol} . *Astron. Astrophys.* **2024**, *691*, A163. [\[CrossRef\]](#)
141. Maccagni, F.M.; de Blok, W.J.G.; Mancera Piña, P.E.; Ragusa, R.; Iodice, E.; Spavone, M.; McGaugh, S.; Oman, K.A.; Oosterloo, T.A.; Koribalski, B.S.; et al. MHONGOOSE discovery of a gas-rich low surface brightness galaxy in the Dorado group. *Astron. Astrophys.* **2024**, *690*, A69. [\[CrossRef\]](#)
142. de Vaucouleurs, G.; de Vaucouleurs, A.; Corwin, H.G., Jr.; Buta, R.J.; Paturel, G.; Fouque, P. *Third Reference Catalogue of Bright Galaxies*; Springer: Berlin/Heidelberg, Germany, 1991.
143. Haynes, M.P.; Giovanelli, R.; Roberts, M.S. A detailed examination of the neutral hydrogen distribution in the Leo triplet NGC 3632, 3627, and 3628. *Astrophys. J.* **1979**, *229*, 83–90. [\[CrossRef\]](#)
144. Soida, M.; Urbanik, M.; Beck, R.; Wielebinski, R.; Balkowski, C. Unusual magnetic fields in the interacting spiral NGC 3627. *Astron. Astrophys.* **2001**, *378*, 40–50. [\[CrossRef\]](#)
145. Moustakas, J.; Kennicutt, R.C.; Tremonti, C.A.; Dale, D.A.; Smith, J.D.; Calzetti, D. Optical Spectroscopy and Nebular Oxygen Abundances of the Spitzer/SINGS Galaxies. *Astrophys. J. Suppl.* **2010**, *190*, 233–266. [\[CrossRef\]](#)
146. Casasola, V.; Hunt, L.K.; Combes, F.; García-Burillo, S.; Neri, R. Molecular Gas in NUClei of GALaxies (NUGA). XIV. The barred LINER/Seyfert 2 galaxy NGC 3627. *Astron. Astrophys.* **2011**, *527*, A92. [\[CrossRef\]](#)
147. Kim, T.; Gadotti, D.A.; Querejeta, M.; Pérez, I.; Zurita, A.; Neumann, J.; van de Ven, G.; Méndez-Abreu, J.; de Lorenzo-Cáceres, A.; Sánchez-Blázquez, P.; et al. Impacts of Bar-driven Shear and Shocks on Star Formation. *Astrophys. J.* **2024**, *968*, 87. [\[CrossRef\]](#)
148. Lomaeva, M.; Saintonge, A.; De Looze, I. The recent star formation histories of nearby galaxies on resolved scales. *Not. R. Astron. Soc.* **2024**, *531*, 815–829. [\[CrossRef\]](#)
149. Leroy, A.K.; Hughes, A.; Liu, D.; Pety, J.; Rosolowsky, E.; Saito, T.; Schinnerer, E.; Schrubba, A.; Usero, A.; Faesi, C.M.; et al. PHANGS-ALMA Data Processing and Pipeline. *Astrophys. J. Suppl.* **2021**, *255*, 19. [\[CrossRef\]](#)
150. Makarov, D.; Prugniel, P.; Terekhova, N.; Courtois, H.; Vauglin, I. HyperLEDA. III. The catalogue of extragalactic distances. *Astron. Astrophys.* **2014**, *570*, A13. [\[CrossRef\]](#)
151. Kalita, B.S.; Silverman, J.D.; Daddi, E.; Bottrell, C.; Ho, L.C.; Ding, X.; Yang, L. A Rest-frame Near-IR Study of Clumps in Galaxies at $1 < z < 2$ Using JWST/NIRCam: Connection to Galaxy Bulges. *Astrophys. J.* **2024**, *960*, 25. [\[CrossRef\]](#)
152. Kalita, B.S.; Silverman, J.D.; Daddi, E.; Mercier, W.; Ho, L.C.; Ding, X. Near-IR clumps and their properties in high- z galaxies with JWST/NIRCam. *Not. R. Astron. Soc.* **2025**, *537*, 402–418. [\[CrossRef\]](#)
153. Freeman, K.C. On the Disks of Spiral and S0 Galaxies. *Astrophys. J.* **1970**, *160*, 811. [\[CrossRef\]](#)
154. Sersic, J.L. *Atlas de Galaxias Australes*; NASA: Washington, DC, USA, 1968.
155. Papaderos, P.; Breda, I.; Humphrey, A.; Michel Gomes, J.; Ziegler, B.L.; Pappalardo, C. Inside-out star formation quenching and the need for a revision of bulge-disk decomposition concepts for spiral galaxies. *Astron. Astrophys.* **2022**, *658*, A74. [\[CrossRef\]](#)
156. Schwarz, G. Estimating the Dimension of a Model. *Ann. Stat.* **1978**, *6*, 461–464. [\[CrossRef\]](#)
157. Bailer-Jones, C.A.L. *Practical Bayesian Inference*; Cambridge University Press: Cambridge, UK, 2017.
158. Simard, L.; Mendel, J.T.; Patton, D.R.; Ellison, S.L.; McConnachie, A.W. A Catalog of Bulge+disk Decompositions and Updated Photometry for 1.12 Million Galaxies in the Sloan Digital Sky Survey. *Astrophys. J. Suppl.* **2011**, *196*, 11. [\[CrossRef\]](#)
159. Head, J.T.C.G.; Lucey, J.R.; Hudson, M.J.; Smith, R.J. Dissecting the red sequence: The bulge and disc colours of early-type galaxies in the Coma cluster. *Not. R. Astron. Soc.* **2014**, *440*, 1690–1711. [\[CrossRef\]](#)

160. Ramambason, L.; Lebouteiller, V.; Bik, A.; Richardson, C.T.; Galliano, F.; Schaerer, D.; Morisset, C.; Polles, F.L.; Madden, S.C.; Chevance, M.; et al. Inferring the HII region escape fraction of ionizing photons from infrared emission lines in metal-poor star-forming dwarf galaxies. *Astron. Astrophys.* **2022**, *667*, A35. [\[CrossRef\]](#)
161. Katsioli, S.; Adam, R.; Ade, P.; Ajeddig, H.; André, P.; Artis, E.; Aussel, H.; Beelen, A.; Benoît, A.; Berta, S.; et al. Exploring the millimetre emission in nearby galaxies: Analysis of the edge-on galaxy NGC 891. *Eur. Phys. J. Web Conf.* **2022**, *257*, 00023. [\[CrossRef\]](#)
162. Katsioli, S.; Xilouris, E.M.; Kramer, C.; Adam, R.; Ade, P.; Ajeddig, H.; André, P.; Artis, E.; Aussel, H.; Baes, M.; et al. The stratification of ISM properties in the edge-on galaxy NGC 891 revealed by NIKA2. *Astron. Astrophys.* **2023**, *679*, A7. [\[CrossRef\]](#)
163. Pantoni, L.; Adam, R.; Ade, P.; Ajeddig, H.; André, P.; Artis, E.; Aussel, H.; Baes, M.; Beelen, A.; Benoît, A.; et al. IAS/CEA Evolution of Dust in Nearby Galaxies (ICED): The spatially-resolved dust properties of NGC4254. *Eur. Phys. J. Web Conf.* **2024**, *293*, 00038. [\[CrossRef\]](#)
164. Bell, A.C.; Onaka, T.; Galliano, F.; Wu, R.; Doi, Y.; Kaneda, H.; Ishihara, D.; Giard, M. Investigation of the origin of the anomalous microwave emission in Lambda Orionis. *Publ. Astron. Soc. Jpn.* **2019**, *71*, 123. [\[CrossRef\]](#)
165. Viaene, S.; Nersesian, A.; Fritz, J.; Verstocken, S.; Baes, M.; Bianchi, S.; Casasola, V.; Cassarà, L.; Clark, C.; Davies, J.; et al. High-resolution, 3D radiative transfer modelling. IV. AGN-powered dust heating in NGC 1068. *Astron. Astrophys.* **2020**, *638*, A150. [\[CrossRef\]](#)
166. Stalevski, M.; Fritz, J.; Baes, M.; Nakos, T.; Popović, L.Č. 3D radiative transfer modelling of the dusty tori around active galactic nuclei as a clumpy two-phase medium. *Not. R. Astron. Soc.* **2012**, *420*, 2756–2772. [\[CrossRef\]](#)
167. Hönig, S.F.; Beckert, T.; Ohnaka, K.; Weigelt, G. Radiative transfer modeling of three-dimensional clumpy AGN tori and its application to NGC 1068. *Astron. Astrophys.* **2006**, *452*, 459–471. [\[CrossRef\]](#)
168. de Vaucouleurs, G. Recherches sur les Nebuleuses Extragalactiques. *Ann. D’Astrophys.* **1948**, *11*, 247.
169. Sauvage, M.; Sacchi, N.; Bendo, G.J.; Boselli, A.; Pohlen, M.; Wilson, C.D.; Auld, R.; Baes, M.; Barlow, M.J.; Bock, J.J.; et al. The central region of spiral galaxies as seen by Herschel. M 81, M 99, and M 100. *Astron. Astrophys.* **2010**, *518*, L64. [\[CrossRef\]](#)
170. Pessa, I.; Schinnerer, E.; Sanchez-Blazquez, P.; Belfiore, F.; Groves, B.; Emsellem, E.; Neumann, J.; Leroy, A.K.; Bigiel, F.; Chevance, M.; et al. Resolved stellar population properties of PHANGS-MUSE galaxies. *Astron. Astrophys.* **2023**, *673*, A147. [\[CrossRef\]](#)
171. Savchenko, S.S.; Reshetnikov, V.P. Pitch angle variations in spiral galaxies. *Not. R. Astron. Soc.* **2013**, *436*, 1074–1083. [\[CrossRef\]](#)
172. Marchuk, A.A.; Mosenkov, A.V.; Chugunov, I.V.; Kostiuk, V.S.; Skryabina, M.N.; Reshetnikov, V.P. A new, purely photometric method for determination of resonance locations in spiral galaxies. *Not. R. Astron. Soc.* **2024**, *527*, L66–L70. [\[CrossRef\]](#)
173. Martínez-García, E.E.; González-Lópezlira, R.A.; Gómez, G.C. Effects of Non-Circular Motions on Azimuthal Color Gradients. *Astrophys. J.* **2009**, *707*, 1650–1658. [\[CrossRef\]](#)
174. Sakhibov, F.; Gusev, A.S.; Hemmerich, C. Azimuthal propagation of star formation in nearby spiral galaxies: NGC 628, NGC 3726, and NGC 6946. *Not. R. Astron. Soc.* **2021**, *508*, 912–925. [\[CrossRef\]](#)
175. Yu, S.Y.; Ho, L.C. Dependence of the Spiral Arms Pitch Angle on Wavelength as a Test of the Density Wave Theory. *Astrophys. J.* **2018**, *869*, 29. [\[CrossRef\]](#)
176. Martínez-García, E.E.; González-Lópezlira, R.A.; Puerari, I. Colour jumps across the spiral arms of Hubble Ultra Deep Field galaxies. *Not. R. Astron. Soc.* **2023**, *524*, 18–31. [\[CrossRef\]](#)
177. Kennicutt, R.C., Jr. The shapes of spiral arms along the Hubble sequence. *Astron. J.* **1981**, *86*, 1847–1858. [\[CrossRef\]](#)
178. Higdon, J.L.; Wallin, J.F. A Minor-Merger Interpretation for NGC 1097’s “Jets”. *Astrophys. J.* **2003**, *585*, 281–297. [\[CrossRef\]](#)
179. Elagali, A.; Staveley-Smith, L.; Rhee, J.; Wong, O.I.; Bosma, A.; Westmeier, T.; Koribalski, B.S.; Heald, G.; For, B.Q.; Kleiner, D.; et al. WALLABY early science—III. An H I study of the spiral galaxy NGC 1566. *Not. R. Astron. Soc.* **2019**, *487*, 2797–2817. [\[CrossRef\]](#)
180. de Blok, W.J.G.; Walter, F.; Brinks, E.; Trachternach, C.; Oh, S.H.; Kennicutt, R.C., Jr. High-Resolution Rotation Curves and Galaxy Mass Models from THINGS. *Astron. J.* **2008**, *136*, 2648–2719. [\[CrossRef\]](#)
181. Foyle, K.; Rix, H.W.; Dobbs, C.L.; Leroy, A.K.; Walter, F. Observational Evidence Against Long-lived Spiral Arms in Galaxies. *Astrophys. J.* **2011**, *735*, 101. [\[CrossRef\]](#)
182. Kostiuk, V.; Marchuk, A.; Gusev, A.; Chugunov, I. A Comprehensive Analysis on the Nature of the Spiral Arms in NGC 3686, NGC 4321, and NGC 2403. *Galaxies* **2025**, *13*, 27. [\[CrossRef\]](#)
183. Oh, S.H.; Kim, W.T.; Lee, H.M.; Kim, J. Physical Properties of Tidal Features in Interacting Disk Galaxies. *Astrophys. J.* **2008**, *683*, 94–113. [\[CrossRef\]](#)
184. Kostiuk, V.S.; Marchuk, A.A.; Gusev, A.S. Cross-method Analysis of Corotation Radii Data Set for Spiral Galaxies. *Res. Astron. Astrophys.* **2024**, *24*, 075007. [\[CrossRef\]](#)
185. Tremaine, S.; Weinberg, M.D. A kinematic method for measuring the pattern speed of barred galaxies. *Astrophys. J.* **1984**, *282*, L5–L7. [\[CrossRef\]](#)
186. Font, J.; Beckman, J.E.; Querejeta, M.; Epinat, B.; James, P.A.; Blasco-herrera, J.; Erroz-Ferrer, S.; Pérez, I. Interlocking Resonance Patterns in Galaxy Disks. *Astrophys. J. Suppl.* **2014**, *210*, 2. [\[CrossRef\]](#)

187. Garcia-Burillo, S.; Combes, F.; Schinnerer, E.; Boone, F.; Hunt, L.K. Molecular gas in NUClei of GALaxies (NUGA). IV. Gravitational torques and AGN feeding. *Astron. Astrophys.* **2005**, *441*, 1011–1030. [[CrossRef](#)]
188. Williams, T.G.; Schinnerer, E.; Emsellem, E.; Meidt, S.; Querejeta, M.; Belfiore, F.; Bešlić, I.; Bigiel, F.; Chevance, M.; Dale, D.A.; et al. Applying the Tremaine-Weinberg Method to Nearby Galaxies: Stellar-mass-based Pattern Speeds and Comparisons with ISM Kinematics. *Astron. J.* **2021**, *161*, 185. [[CrossRef](#)]
189. Elmegreen, D.M.; Elmegreen, B.G. Inner Two-Arm Symmetry in Spiral Galaxies. *Astrophys. J.* **1995**, *445*, 591. [[CrossRef](#)]
190. Lin, L.H.; Wang, H.H.; Hsieh, P.Y.; Taam, R.E.; Yang, C.C.; Yen, D.C.C. Hydrodynamical Simulations of the Barred Spiral Galaxy NGC 1097. *Astrophys. J.* **2013**, *771*, 8. [[CrossRef](#)]
191. Font, J.; Beckman, J.E.; Zaragoza-Cardiel, J.; Fathi, K.; Epinat, B.; Amram, P. The ratio of pattern speeds in double-barred galaxies. *Not. R. Astron. Soc.* **2014**, *444*, L85–L89. [[CrossRef](#)]
192. Piñol-Ferrer, N.; Fathi, K.; Carignan, C.; Font, J.; Hernandez, O.; Karlsson, R.; van de Ven, G. Bar pattern speed and position of the circumnuclear ring in NGC 1097. *Not. R. Astron. Soc.* **2014**, *438*, 971–982. [[CrossRef](#)]
193. Ruiz-García, M.; Querejeta, M.; García-Burillo, S.; Emsellem, E.; Meidt, S.E.; Sormani, M.C.; Schinnerer, E.; Williams, T.G.; Bazzi, Z.; Colombo, D.; et al. Dynamical resonances in PHANGS galaxies. *Astron. Astrophys.* **2024**, *691*, A351. [[CrossRef](#)]
194. Vera-Villamizar, N.; Dottori, H.; Puerari, I.; de Carvalho, R. Analysis of Resonances in Grand Design Spiral Galaxies. *Astrophys. J.* **2001**, *547*, 187–199. [[CrossRef](#)]
195. Abdeen, S.; Kenefick, D.; Kenefick, J.; Miller, R.; Shields, D.W.; Monson, E.B.; Davis, B.L. Determining the co-rotation radii of spiral galaxies using spiral arm pitch angle measurements at multiple wavelengths. *Not. R. Astron. Soc.* **2020**, *496*, 1610–1619. [[CrossRef](#)]
196. Rand, R.J.; Wallin, J.F. Pattern Speeds of BIMA SONG Galaxies with Molecule-dominated Interstellar Mediums Using the Tremaine-Weinberg Method. *Astrophys. J.* **2004**, *614*, 142–157. [[CrossRef](#)]
197. Marchuk, A.A. Resonance coupling in spiral arms. Patterns for flat rotation curve. *Astron. Astrophys.* **2024**, *686*, L14. [[CrossRef](#)]
198. Korchagin, V.; Kikuchi, N.; Miyama, S.M.; Orlova, N.; Peterson, B.A. Global Spiral Modes in NGC 1566: Observations and Theory. *Astrophys. J.* **2000**, *541*, 565–578. [[CrossRef](#)]
199. van der Giessen, S.A.; Matsumoto, K.; Relano, M.; De Looze, I.; Romano, L.; Hirashita, H.; Nagamine, K.; Baes, M.; Palla, M.; Hou, K.C.; et al. Radial properties of dust in galaxies: Comparison between observations and isolated galaxy simulations. *Astron. Astrophys.* **2024**, *692*, A39. [[CrossRef](#)]
200. De Looze, I.; Lamperti, I.; Saintonge, A.; Relaño, M.; Smith, M.W.L.; Clark, C.J.R.; Wilson, C.D.; Declair, M.; Jones, A.P.; Kennicutt, R.C.; et al. JINGLE—IV. Dust, H I gas, and metal scaling laws in the local Universe. *Not. R. Astron. Soc.* **2020**, *496*, 3668–3687. [[CrossRef](#)]
201. Matsumoto, K.; Hirashita, H.; Nagamine, K.; van der Giessen, S.; Romano, L.E.C.; Relaño, M.; De Looze, I.; Baes, M.; Nersesian, A.; Camps, P.; et al. Observational signatures of the dust size evolution in isolated galaxy simulations. *Astron. Astrophys.* **2024**, *689*, A79. [[CrossRef](#)]
202. Egorov, O.V.; Kreckel, K.; Sandstrom, K.M.; Leroy, A.K.; Glover, S.C.O.; Groves, B.; Kruijssen, J.M.D.; Barnes, A.T.; Belfiore, F.; Bigiel, F.; et al. PHANGS-JWST First Results: Destruction of the PAH Molecules in H II Regions Probed by JWST and MUSE. *Astrophys. J.* **2023**, *944*, L16. [[CrossRef](#)]
203. Vorobyov, E.I.; Shchekinov, Y.A. Radial transport of dust in spiral galaxies. *New Astron.* **2006**, *11*, 240–255. [[CrossRef](#)]
204. Scarano, S.; Lépine, J.R.D. Radial metallicity distribution breaks at corotation radius in spiral galaxies. *Not. R. Astron. Soc.* **2013**, *428*, 625–640. [[CrossRef](#)]
205. Gontcharov, G.A. Spatial variations of the extinction law in the galactic disk from infrared observations. *Astron. Lett.* **2013**, *39*, 83–94. [[CrossRef](#)]
206. Aramyan, L.S.; Hakobyan, A.A.; Petrosian, A.R.; de Lapparent, V.; Bertin, E.; Mamon, G.A.; Kunth, D.; Nazaryan, T.A.; Adibekyan, V.; Turatto, M. Supernovae and their host galaxies—IV. The distribution of supernovae relative to spiral arms. *Not. R. Astron. Soc.* **2016**, *459*, 3130–3143. [[CrossRef](#)]
207. Foyle, K.; Rix, H.W.; Walter, F.; Leroy, A.K. Arm and Interarm Star Formation in Spiral Galaxies. *Astrophys. J.* **2010**, *725*, 534–541. [[CrossRef](#)]

Disclaimer/Publisher’s Note: The statements, opinions and data contained in all publications are solely those of the individual author(s) and contributor(s) and not of MDPI and/or the editor(s). MDPI and/or the editor(s) disclaim responsibility for any injury to people or property resulting from any ideas, methods, instructions or products referred to in the content.